CrossMark

The Nuclear Reaction Network WinNet

M. Reichert[1] , C. Winteler[2], O. Korobkin[3] , A. Arcones[4,5], J. Bliss[4], M. Eichler[4] , U. Frischknecht[2], C. Fröhlich[6] ,
R. Hirschi[7,8] , M. Jacobi[4] , J. Kuske[4], G. Martínez-Pinedo[4,5] , D. Martin[4] , D. Mocelj[2], T. Rauscher[2,9] , and
F.-K. Thielemann[2,5]

[1] Departament d'Astonomia i Astrofísica, Universitat de València, Edifici d'Investigatció Jeroni Munyoz, C/Dr. Moliner, 50, E-46100 Burjassot (València), Spain
moritz.reichert@uv.es
[2] Department of Physics, University of Basel, Klingelbergstr. 82, CH-4056 Basel, Switzerland
[3] Center for Theoretical Astrophysics, Los Alamos National Laboratory, Los Alamos, NM 87545, USA
[4] Institut für Kernphysik (Theoriezentrum), Technische Universität Darmstadt, Schlossgartenstr. 2, D-64289 Darmstadt, Germany
[5] GSI Helmholtzzentrum für Schwerionenforschung GmbH, Planckstr. 1, D-64291 Darmstadt, Germany
[6] Department of Physics, North Carolina State University, Raleigh, NC 27695, USA
[7] Astrophysics Group, Lennard-Jones Laboratories, Keele University, Keele ST5 5BG, UK
[8] Institute for the Physics and Mathematics of the Universe (WPI), University of Tokyo, 5-1-5 Kashiwanoha, Kashiwa 277-8583, Japan
[9] Centre for Astrophysics Research, University of Hertfordshire, Hatfield AL10 9AB, UK

Abstract

We present the state-of-the-art single-zone nuclear reaction network WINNET, which is capable of calculating the nucleosynthetic yields of a large variety of astrophysical environments and conditions. This ranges from the calculation of the primordial nucleosynthesis, where only a few nuclei are considered, to the ejecta of neutron star mergers with several thousands of involved nuclei. Here we describe the underlying physics and implementation details of the reaction network. We additionally present the numerical implementation of two different integration methods, the implicit Euler method and Gears method, along with their advantages and disadvantages. We furthermore describe basic example cases of thermodynamic conditions that we provide together with the network and demonstrate the reliability of the code by using simple test cases. With this publication, WINNET will be publicly available and open source at GitHub and Zenodo.

1. Introduction

Nuclear reaction networks are crucial to investigate the synthesis of elements and their isotopes in astrophysical events. While the events can vastly differ in their conditions, the procedure to derive their ejecta composition is always similar. The foundation of the understanding of the origin of elements has been outlined already in Alpher et al. (1948), the so-called $\alpha\beta\gamma$ paper.

The field of nucleosynthetic calculations encompasses the production of the light elements during the Big Bang (e.g., Peebles 1966; Wagoner et al. 1967; Yang et al. 1984; Boesgaard & Steigman 1985; Kawano et al. 1988; Olive et al. 1990; Walker et al. 1991; Smith et al. 1993; Cyburt et al. 2016; Coc & Vangioni 2017; Pitrou et al. 2018, 2021; Fields & Olive 2022), the element production during the lifetime of stars (see, e.g., Woosley & Weaver 1995; Arnett 1977; Heger et al. 2003; Heger & Woosley 2010; Maeder & Meynet 2012; Kippenhahn et al. 2013; Karakas & Lattanzio 2014; Frischknecht et al. 2016; Karakas & Lugaro 2016; Bisterzo et al. 2017; Doherty et al. 2017; Gil-Pons et al. 2018; Leung & Nomoto 2018; Limongi & Chieffi 2018; Thielemann et al. 2018a; Arnett et al. 2019; Kaiser et al. 2020; Kobayashi et al. 2020; Leung et al. 2020; Busso et al. 2021; Eggenberger et al. 2021), and more violent explosive events such as classical novae (e.g., Arnould et al. 1980; Wiescher et al. 1986; José et al. 2004; Jose 2016; Vasini et al. 2022), X-ray bursts (e.g., Wiescher et al. 1986; Rembges

et al. 1997; Schatz et al. 1998; Cyburt et al. 2010; Jose 2016; Meisel et al. 2020), type Ia supernovae (e.g., Arnett 1969; Arnett et al. 1971; Iben & Tutukov 1984; Nomoto et al. 1984; Mueller & Arnett 1986; Thielemann et al. 1986; Woosley et al. 1986; Khokhlov et al. 1993; Höflich et al. 1998; Röpke et al. 2012; Hillebrandt et al. 2013; Pakmor et al. 2013; Dan et al. 2015; Maeda & Terada 2016; García-Senz et al. 2016; Jiang et al. 2017; Röpke & Sim 2018; Thielemann et al. 2018b; Shen et al. 2018; Leung & Nomoto 2018; Gronow et al. 2021; Lach et al. 2022), core-collapse supernovae (e.g., Kotake et al. 2012; Burrows 2013; Janka et al. 2016; Müller 2016; Radice et al. 2018; Müller 2020; Vartanyan et al. 2022) with a focus on nucleosynthesis (e.g., Woosley & Weaver 1995; Thielemann et al. 1996; Woosley & Heger 2006; Heger & Woosley 2010; Perego et al. 2015; Sukhbold et al. 2016; Wanajo et al. 2018; Curtis et al. 2019; Witt et al. 2021; Ghosh et al. 2022), or a focus on *r*-process or neutrino-driven winds in supernovae (e.g., Qian & Woosley 1996; Cardall & Fuller 1997; Hoffman et al. 1997; Otsuki et al. 2000; Thompson et al. 2001; Wanajo et al. 2001; Fröhlich et al. 2006b; Kratz et al. 2008; Bliss et al. 2020; Psaltis et al. 2022), magnetorotational supernovae (Nishimura et al. 2006; Winteler et al. 2012; Nishimura et al. 2015, 2017b; Mösta et al. 2018; Halevi & Mösta 2018; Reichert et al. 2021; Powell et al. 2023; Reichert et al. 2023), collapsars (MacFadyen & Woosley 1999; Pruet et al. 2003; Surman & McLaughlin 2004; McLaughlin & Surman 2005; Fujimoto et al. 2008; Siegel et al. 2019; Miller et al. 2020; Zenati et al. 2020; Barnes & Metzger 2022; Just et al. 2022a), and neutron star mergers (e.g., Freiburghaus et al. 1999; Korobkin et al. 2012; Martin et al. 2015; Wu et al. 2016, 2019; Bovard et al. 2017; Lippuner et al. 2017; Holmbeck et al. 2019; Wanajo et al. 2021;

Rosswog 2022; Kullmann et al. 2022, 2023). Without nucleosynthesis calculations, a whole layer of information and observables would remain inaccessible.

Some applications require a complex modeling that takes species diffusion or convective mixing and nuclear burning simultaneously into account (such as, e.g., the oxygen-burning phase of a star or the rapid accreting white dwarfs; Hix & Thielemann 1999; Denissenkov et al. 2019), and the nuclear reaction network must therefore be included in a hydrodynamical simulation. This often has the consequence that only a restricted number of nuclei are considered in the calculation (from the 13 or 14 alpha nuclei network—13 or 14α— developed by Thielemann and used, e.g., in Mueller 1986; Benz et al. 1989; Livne & Arnett 1995; Garcia-Senz et al. 2013; García-Senz et al. 2016) over small quasi-equilibrium networks (e.g., Hix et al. 1998; Timmes et al. 2000; Hix et al. 2007; named QE-reduced or iso7), to slightly enlarged networks beyond 13α—like net21—which include additional neutron-rich isotopes in the Fe group in order to be able to follow Y_e below 0.5 (for a comparison of these approaches, see Bravo 2020). Recently such methods have been extended to networks that contain up to the order of 100 nuclei (Harris et al. 2017; Sandoval et al. 2021; Navó et al. 2023). These so-called in situ networks have the advantage of providing an accurate nuclear energy production as well as more precise nucleon abundances that imply more realistic neutrino opacities for the feedback to the simulation (e.g., Mueller 1986; Nakamura et al. 2014; Harris et al. 2017; Navó et al. 2023). On the other hand, simplifying assumptions within the nuclear reaction network equations, artificial numerical diffusion (e.g., Fryxell et al. 1991; Hix & Thielemann 1999; Plewa & Müller 1999), and the reduced set of nuclei in such energy generation networks can make the predicted ejecta composition, even with extended postprocessing networks, more uncertain (this is nicely shown in Bravo 2020).

For astrophysical scenarios with a much larger diffusion timescale compared to the nuclear burning timescale, one can trace the ejecta with passively advected particles whose movements are influenced by the velocity field of the fluid (e.g., Nagataki et al. 1997; Seitenzahl et al. 2010; Nishimura et al. 2015; Harris et al. 2017; Bovard & Rezzolla 2017; Sieverding et al. 2023). These so-called tracer particles record the thermodynamic conditions as well as the neutrino fluxes in time. In the case that the impact of diffusion on the composition is negligible compared to the burning, each tracer can be calculated individually, and the total ejected matter is the (possibly weighted) average over all tracer particles individually. Reaction networks that are based on individual tracers (or zones) that are unable to interact with each other are called single-zone nuclear reaction networks. The advantage of those codes is that they can include a much more complete set of nuclei and reactions. This enables a calculation of the synthesis of the heaviest known elements, typically with ~7000 nuclei and ~90,000 reactions involved.

The compilation of a consistent reaction database is especially challenging. Nuclear reactions are often provided in different formats and in different databases that are individually complete. Among others, the largest and publicly available databases are the JINA Reaclib database (Cyburt et al. 2010), Bruslib (Aikawa et al. 2005), the Starlib database (Sallaska et al. 2013), NACRE (Xu et al. 2013), and KADONIS (Dillmann et al. 2006). However, none of the

aforementioned libraries provides a complete set of electron/positron captures as well as β^+/β^- decays at stellar conditions (Fuller et al. 1982, 1985; Oda et al. 1994; Langanke & Martínez-Pinedo 2001; Pruet & Fuller 2003; Suzuki et al. 2016), neutrino reactions (e.g., Bruenn 1986; Langanke & Kolbe 2002; Fröhlich et al. 2006b; Sieverding et al. 2018, 2019), or fission reactions and fragment distributions (Panov et al. 2005; Goriely et al. 2009; Panov et al. 2010; Petermann et al. 2012; Eichler et al. 2015; Vassh et al. 2019). For an almost complete survey of all of these resources, see the JINAWEB collected list.[10] Therefore, nuclear reaction networks always have to perform a certain amount of merging of the reaction rates if one wants to use a complete as possible set of reaction rates. Doing this rigorously can be a major task, as the consistency depends not only on not adding reactions twice or leaving them out, but also on adding reactions with the same underlying nuclear input, such as the same nuclear masses, which, far from stable nuclei, are theoretically calculated.

From a numerical point of view, reaction networks can be challenging as well. The huge differences in timescales of the reaction rates (e.g., weak decays versus strong reactions) introduce a stiffness into the differential equations. As a consequence, explicit integration methods become unstable, and implicit methods have to be applied. A full implicit implementation was first achieved by Truran et al. (1966b, 1967), Arnett & Truran (1969), Woosley et al. (1973), Arnould (1976), and Thielemann et al. (1979). While nowadays usually the first-order implicit Euler scheme is used within large nuclear reaction networks, tests with higher-order implicit schemes such as the Gear scheme have been performed as well (e.g., Timmes 1999; Longland et al. 2014).

A variety of single-zone reaction networks with fully implicit schemes exist in the literature, e.g., the SantaCruz-code by the Woosley group, going back to Woosley et al. (1973), which followed Arnett (1969) and Truran et al. (1966a) introducing a complete Newton–Raphson scheme, BASNET (Thielemann et al. 1979; for an early comparison of the two codes and the implemented reaction rate libraries, see Hoffman et al. 1999), XNET (Hix & Thielemann 1999), RNET (Wanajo et al. 2001), CFNET (Fröhlich et al. 2006a), NUCNET (Meyer & Adams 2007), RJAVA (Kostka et al. 2014), TORCH (Paxton et al. 2015), GSINET (Mendoza-Temis et al. 2015), SKYNET (Lippuner & Roberts 2017), PRISM (Mumpower et al. 2018; Sprouse et al. 2021), PYNUCASTRO (Smith et al. 2023), and other unnamed reaction networks (e.g., Timmes 1999; Iliadis et al. 2002; Otsuki et al. 2003; Koike et al. 2004; Goriely et al. 2011).[11] However, only a small subset of them is publicly available, among them PYNUCASTRO,[12] TORCH,[13] RJAVA,[14] NUCNET,[15] XNET,[16] and SKYNET.[17]

Here we present the single-zone nuclear reaction network code WINNET, an updated version of the reaction network that has been first used in the context of Big Bang nucleosynthesis in Vonlanthen et al. (2009) and later for calculating the synthesis of heavy elements in Winteler et al. (2012). WINNET

---

[10] https://www.jinaweb.org/science-research/scientific-resources/data
[11] See also https://cococubed.com/code_pages/burn.shtml.
[12] https://github.com/pynucastro/pynucastro/
[13] https://cococubed.com/code_pages/net_torch.shtml
[14] http://quarknova.ca/rJava/index.html
[15] https://sourceforge.net/u/mbradle/blog/
[16] https://github.com/starkiller-astro/XNet
[17] https://bitbucket.org/jlippuner/skynet/

has a common origin to many other previously mentioned reaction networks such as XNET, CFNET, and GSINET as all of them were influenced by BASNET, which served as an initial template.

WINNET had been already used for different astrophysics problems; however, it was not publicly available. The code has been entirely written in Fortran 90 and has a user-friendly interface. WINNET is able to merge reaction rates from multiple sources and is designed for high-performance computations. It includes two fully implicit schemes, the first-order implicit Euler-backward scheme and the higher-order Gear scheme. This paper presents the basics of nuclear reaction networks as well as provides insight of the implementations within WINNET.

In Section 2 we present the fundamental physic concepts for nuclear reaction networks. This includes the derivation of the ordinary differential equation (ODE) that is solved in WINNET (Section 2.1), the principle of detailed balance (Section 2.2), the concept of nuclear statistical equilibrium (NSE; Section 2.3), a method to account for nuclear energy generation within the temperature evolution (Section 2.4), and the treatment of Coulomb corrections (Section 2.5). The code structure and included numerical solvers are presented in Section 3. The different supported reaction rate formats are introduced in Section 4. Applications and test cases are presented in Section 5. We close with a summary in Section 6.

2. Nuclear Reaction Network Fundamentals

2.1. Nuclear Reaction Networks

The fundamental theory behind nuclear reaction networks reaches back far into the past (see, e.g., Clayton 1968; Truran et al. 1966a; Arnett & Truran 1969; Woosley et al. 1973; Hix & Thielemann 1999; Hix & Meyer 2006; Winteler et al. 2012; Lippuner & Roberts 2017). Here we repeat briefly how to derive the differential equations, but refer the reader to previous publications for more details.

The cross section of a reaction

$$\sigma = \frac{\text{number of reactions per target and second}}{\text{flux of incoming particles}}, \quad (1)$$

is related to the probability of a nucleus i to react with nucleus j. If (e.g., in laboratory conditions like accelerator experiments) the relative velocity between target i and projectile j is a constant value v, it is given by

$$\sigma = \frac{r/n_i}{n_j v}. \quad (2)$$

Here, r is the number of reactions per volume and time, n_i and n_j are the number densities of the target and projectile, respectively. In an astrophysical plasma, both target and projectile follow specific velocity distributions depending on the environmental conditions like temperature and density (and the reaction cross section is that of a target with thermally populated excited states; e.g., Fowler 1974; Holmes et al. 1976; Rauscher & Thielemann 2000; Rauscher 2022). For an arbitrary velocity distribution, r can be expressed as:

$$r_{i,j} = \int \sigma(|v_i - v_j|) \cdot |v_i - v_j| dn_i dn_j. \quad (3)$$

In thermal equilibrium, the velocity (or momentum or energy) distribution depends on the type of particle, i.e., photons obey a Planck distribution and nuclei obey, in most cases, a Maxwell–Boltzmann distribution. Therefore, for photons, dn_γ is given by

$$dn_\gamma = \frac{1}{\pi^2(c\hbar)^3} \frac{E_\gamma^2}{\exp[E_\gamma/(k_B T)] - 1} dE_\gamma \quad (4)$$

and for nuclei dn_i is expressed by

$$dn_i = n_i \left(\frac{m_i}{2\pi k_B T}\right)^{3/2} \exp\left(-\frac{m_i v_i^2}{2k_B T}\right) d^3 v_i \equiv n_i \phi(v_i)\, d^3 v_i, \quad (5)$$

where m_i is the nuclear mass. For reactions between a nucleus and a photon, r is therefore given by

$$r_{i,\gamma} = \frac{n_i}{\pi^2 c^2 \hbar^3} \int_0^\infty \frac{\sigma(E_\gamma) E_\gamma^2}{\exp[E_\gamma/(k_B T)] - 1} dE_\gamma \equiv n_i\, \lambda_{i,\gamma}(T). \quad (6)$$

Reactions of this type are called photodisintegrations. For the case of two nuclei, the r is given by

$$r_{i,j} = n_i n_j \int \sigma(|v_i - v_j|) \times |v_i - v_j| \phi(v_i)\phi(v_j) d^3 v_i d^3 v_j$$
$$= n_i n_j \langle \sigma v \rangle_{i,j}, \quad (7)$$

where $\langle \sigma v \rangle_{i,j}$ stands for the product σv integrated over thermal distributions. Furthermore, an additional factor has to be introduced to avoid double counting of identical project and target nuclei. Equation (7) becomes

$$r_{i,j} = \frac{1}{1 + \delta_{ij}} n_i n_j \langle \sigma v \rangle_{i,j} \quad (8)$$

with the delta in the usual sense, i.e., $\delta_{i,j} = 1$ for $i = j$; otherwise, $\delta_{i,j} = 0$. We get

$$r_{j,k,l} = \frac{1}{1 + \delta_{jk} + \delta_{kl} + \delta_{jl} + 2\delta_{jkl}} n_j n_k n_l \langle ijk \rangle$$
$$\equiv \frac{1}{1 + \Delta_{jkl}} n_j n_k n_l \langle ijk \rangle. \quad (9)$$

in case of three participating nuclei, where $\langle ijk \rangle$ stands for three-body reactions (in most cases, a sequence of two two-body reactions and an intermediate reaction product with an extremely short half-life; see, e.g., Nomoto et al. 1985; Görres et al. 1995). For example, the triple α reaction, which describes the probability of three helium nuclei to form ^{12}C, has a pre-factor of $1/(1 + \Delta_{jkl}) = 1/6$.

Within a fluid that moves with velocity v, n_i does not only change by nuclear reactions but also by the net-flow into the volume. We have

$$\frac{\partial n_i}{\partial t} = -\nabla \cdot (n_i v) + \sum_j N_j^i r_j + \sum_{j,k} N_{j,k}^i r_{j,k}$$
$$+ \sum_{j,k,l} N_{j,k,l}^i r_{j,k,l}$$
$$=: -\nabla \cdot (n_i v) + C_{\text{nuc}}, \quad (10)$$

where we introduced the factors $N_j^i, N_{j,k}^i, N_{j,k,l}^i$ that account for the number of particles i that gets destroyed (negative) or created (positive) in the reaction. The first term in the equation,

$-\boldsymbol{\nabla} \cdot (n_i \boldsymbol{v})$, accounts for changes due to the fluid flow with velocity $\boldsymbol{v}$, and the last term C_{nuc} accounts for changes due to nuclear reactions. We can reformulate the previous equation by using the Lagrangian time derivative that is related to the Eulerian time derivative via

$$\frac{D}{Dt} = \frac{\partial}{\partial t} + \boldsymbol{v} \cdot \boldsymbol{\nabla}. \tag{11}$$

We can therefore obtain

$$\frac{\partial n_i}{\partial t} = \frac{Dn_i}{Dt} - \boldsymbol{v} \cdot \boldsymbol{\nabla} n_i, \tag{12}$$

and, as a consequence, Equation (10) becomes

$$\frac{Dn_i}{Dt} = -n_i \boldsymbol{\nabla} \cdot \boldsymbol{v} + C_{\mathrm{nuc}}. \tag{13}$$

Using the continuity equation and the Lagrangian time derivative

$$\frac{\partial \rho}{\partial t} = -\boldsymbol{\nabla} \cdot (\rho \boldsymbol{v}) = -\boldsymbol{v} \cdot \boldsymbol{\nabla}\rho - \rho \boldsymbol{\nabla} \cdot \boldsymbol{v} \Rightarrow \frac{D\rho}{Dt} = -\rho \boldsymbol{\nabla} \cdot \boldsymbol{v}, \tag{14}$$

and therefore

$$\boldsymbol{\nabla} \cdot \boldsymbol{v} = -\frac{1}{\rho}\frac{D\rho}{Dt}. \tag{15}$$

Thus, we can insert into Equation (13) and get

$$\frac{Dn_i}{Dt} - \frac{n_i}{\rho}\frac{D\rho}{Dt} = \rho \frac{D(n_i/\rho)}{Dt} = C_{\mathrm{nuc}}. \tag{16}$$

This derivation has been done previously (see, e.g., Mihalas & Weibel-Mihalas 1999) in the context of atomic processes related to radiation transport, but as shown here it is also valid in the context of nuclear reactions (see also Lippuner & Roberts 2017).

In order to obtain a density-independent expression instead of utilizing number densities n_i, we introduce the density (or mass) fraction of nucleus i, X_i, which can be expressed via

$$X_i = \frac{\rho_i}{\rho} = \frac{n_i m_i}{\rho} = \frac{n_i \mathcal{A}_i m_u}{\rho} \approx \frac{n_i A_i m_u}{\rho}. \tag{17}$$

This includes the mass of nuclei $\mathcal{A}_i m_u$ (where $\mathcal{A}_i$ is the relative atomic mass, which can be with a permille error approximated by A_i, the mass number of nucleus i, and $m_u = m(^{12}\mathrm{C})/12$ is the atomic mass unit). Alternatively, one can introduce an abundance, without the inclusion of the weight or mass of a nucleus, as the fraction of the number density of nucleus i in comparison to the total number density of nucleons, approximated by $n = \rho/m_u$, that is conserved by nuclear reactions

$$Y_i = \frac{n_i}{n} = \frac{n_i}{\rho/m_u} = \frac{X_i}{A_i} = \frac{n_i}{\rho N_A} N_A m_u. \tag{18}$$

This definition seems to differ from the traditionally utilized one in nucleosynthesis literature, introduced by Fowler et al. (1967)

$$Y_i = \frac{n_i}{\rho N_A}, \tag{19}$$

as it includes the Avogadro constant N_A rather than the nuclear mass unit m_u. Equations (19) and (18) differ by the product $M_u = N_A m_u$, the molar gas constant, which had until 2019 the

value 10^{-3} kg mol^{-1} or 1 g mol^{-1} in cgs units, leading in Equation (19) to an abundances measure in moles per gram and in Equation (18) to a dimensionless number.

When utilizing the present values of the natural constants (see Table XXXI in Tiesinga et al. 2021) with $N_A = 6.02214076 \times 10^{23}$ mol^{-1} (exact) and $m_u = m(^{12}\mathrm{C})/12 = 1.6605390660(50) \times 10^{-24}$ g with a relative uncertainty of 3×10^{-10}, one obtains for the molar mass constant $M_u = N_A m_u = 0.99999999965(30)$ g mol^{-1}, i.e., equal to 1 with an uncertainty of 3×10^{-10}. Thus, both expressions are numerically identical with an extremely high accuracy in cgs units. However, the different dimensions of Equations (18) and (19) can introduce some confusion (see also Rauscher 2020). In this paper, we continue to utilize the traditional definition for abundances (Equation (19)), but in agreement with Equation (17) and $Y_i = X_i/A_i$ we will treat mass fractions X_i as well as abundances Y_i as dimensionless numbers. When expressing the number densities n_i in terms of abundances Y_i, Equation (16) leads to the form

$$\begin{aligned}\dot{Y}_i = \frac{DY_i}{Dt} = &\sum_j N_j^i \lambda_j Y_j \quad \text{(1-body)} \\ &+ \sum_{j,k} \frac{N_{j,k}^i}{1 + \delta_{jk}} \rho N_A \langle \sigma v \rangle_{j,k} Y_j Y_k \quad \text{(2-body)} \\ &+ \sum_{j,k,l} \frac{N_{j,k,l}^i}{1 + \Delta_{jkl}} \rho^2 N_A^2 \langle ijk \rangle Y_j Y_k Y_l \quad \text{(3-body)}, \end{aligned} \tag{20}$$

where the individual terms can be identified with specific reactions, neglecting reactions involving four or more participants. The first term, standing for one-body reactions, usually includes decays, photodisintegrations, electron or positron captures, and neutrino absorption. The equation is often called the "nuclear reaction network" equation. It is the fundamental differential equation that is solved within WINNET. Note that all ρN_A terms would be replaced by ρ/m_u, when utilizing the alternative definition of abundances Y_i, which would replace N_A by m_u^{-1}.

2.2. Detailed Balance

Reverse or backward reactions have a direct relation to the forward reaction by the so-called detailed balance theorem. We denote as forward reaction those with a positive Q-value defined as the difference between initial and final ground-state masses. The relation between both can be expressed as (e.g., Fowler et al. 1967)

$$\begin{aligned}\langle \sigma v \rangle_{\mathrm{backward}} = &\frac{\Delta_{\mathrm{reactants}}}{\Delta_{\mathrm{products}}}\left(\frac{\prod_{i=1}^{N_{\mathrm{reactants}}} G_i(T)}{\prod_{j=1}^{N_{\mathrm{products}}} G_j(T)}\right) \\ &\times \left(\frac{\prod_{i=1}^{N_{\mathrm{reactants}}} g_i}{\prod_{j=1}^{N_{\mathrm{products}}} g_j}\right)\left(\frac{\prod_{i=1}^{N_{\mathrm{reactants}}} A_i}{\prod_{j=1}^{N_{\mathrm{products}}} A_j}\right)^{3n/2} \\ &\times \left(\frac{m_u k_B T}{2\pi \hbar^2}\right)^{3n/2} \exp\left[-Q/(k_B T)\right]\langle \sigma v \rangle_{\mathrm{forward}}, \end{aligned} \tag{21}$$

where Δ is the double counting factor for reactants/products as in Equation (20), G are the partition functions, g is the spin factor defined as $g = 2J + 1$, where J is the spin of the ground state, A_i is the mass of nucleus i, Q is the Q-value of the reaction, $\langle \sigma v \rangle_{\mathrm{forward}}$ is the cross section of the forward reaction, and n is the difference between the number of reactants and the number of reaction products.

Equation (21) needs to be modified for photodisintegration reactions. There, $\langle \sigma v \rangle_{\mathrm{backward}}$ should be replaced by $\lambda_{\mathrm{backward}}$. In this case, $n \neq 0$, and we therefore get the additional factors that are introduced with n in the exponential in Equation (21). This is consistent with literature (e.g., Fowler et al. 1967) and the Reaclib reverse rates. Therefore, in practice, we can use the above equation for both cases, capture reactions and photo-disintegrations. Equation (21) is also valid for three-body reactions replacing $\langle \sigma v \rangle$ by $\langle ijk \rangle$. It should be mentioned here that the relations in this section include that nuclei in a thermal environment exist with thermally populated excited states.

Within the Jina Reaclib framework, the Q-values are given for each reaction. Additionally, the mass excesses of all nuclei can be found in a separate file (called "winvn"). Ideally, the mass excess is consistent with the Q-value in the Reaclib; however, as pointed out already in Lippuner & Roberts (2017), currently there are inconsistencies between these values. Because the reverse rates in Reaclib use the detailed balance principle with the Q-value from the Reaclib, there can be an inconsistency at the transition of NSE to the network equations caused by the inconsistent Q-values (see Figure 1). Therefore, WINNET is able to calculate detailed balance with the Q-values obtained from the mass excess. We note that there is no optimal solution for this inconsistency. Using the Q-value from the mass excess will make the calculation consistent with NSE, but introduces an inconsistency with the forward rate, as this was calculated on the basis of a different Q-value. Often, it is however more important to be consistent with the equilibrium values. As already mentioned in Lippuner & Roberts (2017), this inconsistency in the Reaclib database may be resolved in the future. However, one philosophy of the JINA Reaclib database is to have up-to-date nuclear masses. Recalculating all reaction rates whenever a new mass is available may not be feasible. To a certain degree, this inconsistency may therefore always be present (H. Schatz 2022, private communication). In any case, the advantage of an on-the-fly calculation of reverse rates is also given when using tabulated rates. For these rates, a tabulation for forward and reverse rates may break the detailed balance principle, and it can be more consistent to calculate the reverse rate based on the tabulation of the forward rate.

2.3. Nuclear Statistical Equilibrium

For high temperatures in explosive environments, typically in excess of about $T \gtrsim 6$ GK, reactions mediated by the strong and electromagnetic interaction are in equilibrium. For these conditions, one can simplify the treatment, replacing the reaction network equations by utilizing an equilibrium approach, which can be expressed in terms of the chemical potentials of the nuclei

$$\mu(Z, N) = N\mu_n + Z\mu_p, \tag{22}$$

where $\mu(Z, N)$ is the chemical potential for a nucleus with mass number $A = Z + N$, μ_n is the chemical potential of neutrons, and μ_p is the chemical potential of protons. For low enough densities, nucleons (fermions) are nondegenerate and therefore
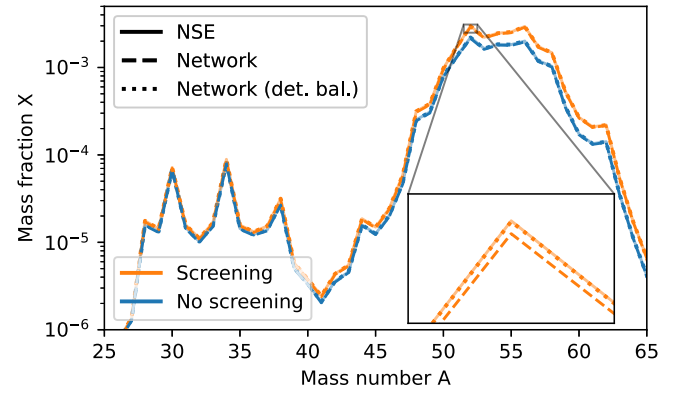
Figure 1. NSE composition with (orange line) and without (blue line) screening corrections in NSE for $T = 7$ GK, $\rho = 10^7$ g cm^{-3}, and $Y_e = 0.5$ (solid lines). Dashed lines show the result of two hydrostatic network runs with and without screening corrections using strong reaction rates from the Jina Reaclib. Dashed lines show the same, but replacing the reverse reactions of the Jina Reaclib with reverse rates that are calculated with detailed balance using the mass excess of the Jina Reaclib. The hydrostatic calculations start with half neutrons and half protons and are calculated for 10^3 s. This illustrates the consistency of the network at NSE transition with and without screening corrections when using the same nuclear masses for the reactions and NSE.

described well by the Maxwell–Boltzmann statistics. Introducing this for the related chemical potentials in Equation (22) leads to the so-called Saha equations (for a detailed derivation of NSE, see, e.g., Hix & Thielemann 1999; Iliadis 2015; Lippuner & Roberts 2017; or for an approach using detailed balance, see, e.g., Clayton 1968):

$$Y(Z, A) = g_{Z,A} G_{Z,A} (\rho N_A)^{A-1} \frac{A^{3/2}}{2^A} \left(\frac{2\pi\hbar}{m_u k_B T} \right)^{\frac{3}{2}(A-1)}$$
$$e^{B_{Z,A}/k_B T} Y_n^{A-Z} Y_p^Z, \tag{23}$$

with the spin factor $g = 2J + 1$, where J is the spin of the ground state, the partition function $G_{Z,A}$, and binding energy of a nucleus $B_{Z,A}$. Furthermore, additional constraints of mass conservation and charge neutrality hold:

$$\sum_i Y_i A_i = 1 \text{ (mass conservation)} \tag{24}$$

$$\sum_i Y_i Z_i = Y_e \text{ (charge neutrality).} \tag{25}$$

This set of equations has two unknowns, namely the abundances of protons Y_p and neutrons Y_n, because temperature, density, and electron fraction are assumed to be known quantities (e.g., from a hydrodynamical simulation). The composition is a function of $Y(\rho, T, Y_e)$ only. In particular, no information of the past behavior is necessary to determine the composition.

Within WINNET, we solve the system of Equations (23), (24), and (25) either with a Newton–Raphson or identical to Smith et al. (2023) the hybrid Powell method from the MINPACK-I package (More et al. 1980) that was translated to Fortran 90 by J. Burkardt.[18] The convergence of the schemes hereby depend often on the initial guess. In WINNET, this guess is obtained by starting to calculate NSE at a high temperature and descending to lower temperatures, taking the results of the higher temperatures as initial value for the lower ones. The

---

initial composition at the starting temperature is assumed to consist of nucleons only with $Y_n = 1 - Y_e$ and $Y_p = Y_e$.

Weak reactions are evolved with a simplified reaction network that includes only these reactions in Equation (20). After a time step, a new electron fraction is determined using Equation (25), and the composition is recomputed assuming for NSE. This assumes that strong and electromagnetic reactions occur instantaneously following a weak reaction consistently with the NSE assumption.

The implementation of screening corrections in NSE is discussed in Section 2.5.

2.4. Nuclear Heating

A proper consideration of the impact of the energy produced by nuclear processes in the hydrodynamical evolution requires the use of an in situ network as discussed in the introduction. However, in postprocessing network calculations, it is commonly assumed that the nuclear energy generation mainly affects the evolution of temperature (see, e.g., Freiburghaus et al. 1999; Mueller 1986; Lippuner & Roberts 2017). In the following, we describe the general description of energy generation and its treatment in WINNET.

The evolution of a fluid element under exchange of heat with the surroundings in a local inertial frame comoving with the fluid is given by the first law of thermodynamics

$$d\varepsilon + pd\left(\frac{1}{n}\right) = \delta q, \qquad (26)$$

where ε is the total energy (including rest-mass energy) per nucleon, and δq is the net heat gained per nucleon. This includes heat produced by shocks or viscous heating or loss by neutrinos when weak processes are considered. Alternatively, if the fluid element is in equilibrium at all times, we have

$$
\begin{aligned}
k_B T ds + \sum_i \mu_i dY_i + \mu_e dY_e &= \delta q \\
&= k_B T ds + \sum_i (\mu_i + Z_i \mu_e) dY_i,
\end{aligned}
\qquad (27)
$$

where s is the entropy per nucleon in units of k_B, and the sum runs over all nuclear species. The term $\mu_e dY_e$ or $Z_i \mu_e dY_i$ accounts for the contribution of electrons and positrons. Typically, the densities we are interested in are such that matter is transparent to neutrinos. To ensure this, within WINNET we include a user-defined parameter to specify the density below which nuclear heating will be taken into account. The energy carried by neutrinos per unit of time can be expressed as

$$\dot{q}_{\text{loss}} = -\sum_i \langle \varepsilon_\nu \rangle^i \lambda_i Y_i, \qquad (28)$$

where $\langle \varepsilon_\nu \rangle^i$ is the average energy of the neutrinos produced by electron capture or β decay of the nucleus i with rate λ_i and abundance Y_i. These quantities are provided in tabulations of weak interaction rates at finite temperature and density (see, e.g., Langanke & Martínez-Pinedo 2001) and in global calculations of β decays for r-process nuclei (Marketin et al. 2016). For measured decays, the average neutrino energies are given by the ENSDF database (Brown et al. 2018).[19] If we

consider only β decays, we can express the average energy $\langle \varepsilon_\nu \rangle^i$ of the neutrinos as a fraction of the β-decay Q-value $Q_{\beta,i}$:

$$\dot{q}_{\text{loss}} = -\sum_i f_{\nu,i} Q_{\beta,i} \lambda_i Y_i. \qquad (29)$$

Assuming that a constant fraction of the energy is carried by neutrinos, we have

$$\dot{q}_{\text{loss}} = -f_\nu \sum_i Q_{\beta,i} \lambda_i Y_i. \qquad (30)$$

A typical value of f_ν for neutron-rich r-process nuclei is $f_\nu = 0.4$ (Marketin et al. 2016), as β decays populate mainly excited states in the daughter nuclei that later decay by either γ or neutron emission. In practice, within WINNET, the average energy of neutrinos produced in the reaction can be taken from all aforementioned sources, and in case of an unknown average neutrino energy, a user-defined f_ν is assumed. Optionally, we also account for escaping thermally produced neutrinos, by, e.g., bremsstrahlung or electron recombination with the analytic fitting formulas of Itoh et al. (1996).[20] Energy cannot only leave the system by neutrinos, but also enter it. When assuming that only neutrino reactions add additional energy to the system, we obtain

$$\dot{q}_{\text{gain}} = \sum_i \langle \varepsilon_\nu \rangle^i \langle \sigma \rangle_i F_\nu Y_i, \qquad (31)$$

where $\langle \varepsilon_\nu \rangle$ is the average energy of the absorbed neutrino, $\langle \sigma \rangle$ is the neutrino average cross section, and F_ν is the neutrino number flux (see Section 4.2.4 for more details about the implementation of neutrino reactions). For the moment, we include ε_ν for charged-current reactions on nucleons only. When combining Equation (27), (30), and (31), we obtain

$$
\begin{aligned}
\dot{s} &= -\frac{1}{k_B T}\left(\sum_i (\mu_i + Z_i \mu_e) \dot{Y}_i - \dot{q} \right) \\
&= -\frac{1}{k_B T}\left(\sum_i (\mu_i + Z_i \mu_e) \dot{Y}_i - (\dot{q}_{\text{loss}} + \dot{q}_{\text{gain}}) \right),
\end{aligned}
\qquad (32)
$$

where we obtain the electron chemical potential from the equation of state (EOS) (Timmes & Arnett 1999), and the chemical potentials of nuclei is given by

$$
\begin{aligned}
\mu_i &= m_i c^2 + k_B T \eta_i \\
\eta_i &= -\ln\left[\frac{g_i G_i(T) m_u}{\rho Y_i} \left(\frac{A_i m_u c^2 k_B T}{2\pi \hbar^2} \right)^{3/2} \right].
\end{aligned}
\qquad (33)
$$

Here m_i is the nuclear mass that we get from the atomic mass excess $\Delta(Z, A)$ by

$$m(Z, A)c^2 = \Delta(Z, A) + A m_u c^2 - Z m_e c^2. \qquad (34)$$

The mass excess from the latest atomic mass evaluation is tabulated in the Jina Reaclib database (Cyburt et al. 2010).

Under NSE conditions, Equation (32) can be expressed as

$$\dot{s} = -\frac{1}{k_B T}[(\mu_p + \mu_e - \mu_n)\dot{Y}_e - \dot{q}], \qquad (35)$$

---

[19] Accessed via the application programming interface of https://www-nds.iaea.org/relnsd/vcharthtml/api_v0_guide.html.

[20] See also https://cococubed.com/code_pages/nuloss.shtml.

showing that only reactions that are not in equilibrium, i.e., weak processes that change Y_e as well as external heating, are responsible for the change in entropy. This result can be also generalized to r-process conditions for which $(n, \gamma) \rightleftarrows (\gamma, n)$ equilibrium is valid. Hence, reactions in equilibrium do not introduce a change in entropy. At high densities, neutrinos are characterized by a chemical potential μ_ν. In this case, one obtains $\dot{s} = -[(\mu_p + \mu_e - \mu_n - \mu_\nu)\dot{Y}_e - \dot{q}]/(k_B T)$, which shows chemical weak equilibrium $\mu_p + \mu_e = \mu_n + \mu_\nu$ corresponds to a maximum of the entropy (Arcones et al. 2010).

Within WINNET, we solve Equation (32) explicitly in a so-called operator splitting method within the same Newton–Raphson as the nuclear network equations (Equation (20)). The initial value of the entropy is determined using the Timmes EOS (Timmes & Arnett 1999). Within every Newton–Raphson iteration, the newly obtained entropy is translated into a temperature via the EOS assuming that the density and composition remain constant. For conditions at which $s \approx 1\text{–}5$ k_B nuc^{-1}, the entropy is dominated by the contribution of nuclei and is very sensitive to the composition. Under these conditions, it is necessary to account for changes in the composition when searching for a new value of the temperature. This is currently not implemented in WINNET.

2.5. Coulomb Corrections

Coulomb effects can significantly influence fusion processes in a hot stellar plasma. Electrons can be attracted by the positive charge of a nucleus and therefore shield and modify the Coulomb interactions between two nuclei. This modifies the nuclear reactions and makes charged particle reactions more likely. The effect can be approximated by correction factors, the so-called screening corrections, which are an important ingredient in nuclear reaction network calculations (e.g., Salpeter 1954). The calculation of the correction factors depends on the temperature and density of the environment (e.g., Salpeter & van Horn 1969; Yakovlev & Shalybkov 1989; Ichimaru 1993; Yakovlev et al. 2006). Usually, three different screening regimes are distinguished: the weak screening, the intermediate screening, and the strong screening regime. The regimes are commonly separated in terms of the ion-coupling parameter (e.g., Kravchuk & Yakovlev 2014)

$$\Gamma_{12} = 2\frac{Z_1 Z_2}{Z_1^{1/3} + Z_2^{1/3}} \frac{e^2 (4\pi n_e)^{1/3}}{3^{1/3} k_B T}$$
$$\approx 4.5494 \times 10^{-4} \frac{Z_1 Z_2}{Z_1^{1/3} + Z_2^{1/3}} (\rho Y_e)^{1/3} T^{-1}, \qquad (36)$$

where T is the temperature in gigakelvin, the electron number density is defined as $n_e = \rho N_A Y_e$, Z_i is the charge of element i, and the elementary charge is e. For lower values of Γ_{12}, the effect of screening becomes smaller. The weak screening regime applies for $\Gamma_{12} \ll 1$, the intermediate regime around $\Gamma_{12} \approx 1$, and the strong regime for larger values. We do not solve the screening corrections numerically, which would be necessary to obtain the corrections for the strong screening regime. Instead, we have implemented a fitted function that was derived within Kravchuk & Yakovlev (2014). They express the so-called screening enhancement factor as (Equation (62) of Kravchuk & Yakovlev 2014)

$$f_{\text{scr}} = \exp\left[\Gamma_{12}\left(b_0 + \frac{5}{8}b_2\zeta^2 + \frac{63}{128}b_4\zeta^4\right)\right], \qquad (37)$$

with ζ defined as

$$\zeta = 3\frac{\Gamma_{12}}{\tau}, \qquad (38)$$

where

$$\tau = \left(\frac{27\pi^2\mu(Z_1 Z_2)^2 e^4}{2k_B T \hbar^2}\right)^{1/3}$$
$$\approx 4.2487 \times \left(\frac{A_1 A_2}{A_1 + A_2}(Z_1 Z_2)^2 \frac{1}{T}\right)^{1/3}, \qquad (39)$$

with the nucleon number A_i and the reduced mass μ. The fitting parameter b_0 is expressed by the difference in Coulomb free energies, which are defined by another fitted function that Kravchuk & Yakovlev (2014) took from Potekhin & Chabrier (2000):

$$f_C(\Gamma) = C_1\left[\sqrt{\Gamma(C_2 + \Gamma)} - C_2 \ln\left(\sqrt{\frac{\Gamma}{C_2}} + \sqrt{1 + \frac{\Gamma}{C_2}}\right)\right]$$
$$+ 2C_3(\sqrt{\Gamma} - \arctan\sqrt{\Gamma})$$
$$+ D_1\left[\Gamma - D_2 \ln\left(1 + \frac{\Gamma}{D_2}\right)\right]$$
$$+ \frac{D_3}{2}\ln\left(1 + \frac{\Gamma^2}{D_4}\right). \qquad (40)$$

Here, $C_1 = -0.907$, $C_2 = 0.62954$, $C_3 = 0.2771$, $D_1 = 0.00456$, $D_2 = 211.6$, $D_3 = -0.0001$, and $D_4 = 0.00462$, and Γ is the ion-coupling parameter for a one-component plasma

$$\Gamma = \frac{Z^{5/3} e^2 (4\pi n_e)^{1/3}}{3^{1/3} k_B T}. \qquad (41)$$

From this, they obtain

$$b_0 = \frac{f_C(\Gamma_1) + f_C(\Gamma_2) - f_C(\Gamma_C)}{\Gamma_{12}}, \qquad (42)$$

where Γ_1 and Γ_2 are the ion-coupling parameters of the reacting nuclei, and Γ_C is the ion-coupling parameter of the compound nucleus. Furthermore, b_2 and b_4 in Equation (37) are defined as

$$b_2 = -\frac{1}{16}\frac{(1 + z^{5/3})^3}{1 + z} \qquad (43)$$

$$b_4 = -\frac{z}{64}\frac{(1 + z^{5/3})^5}{(1 + z)^{11/3}}. \qquad (44)$$

The differences between the screening correction scheme of Kravchuk & Yakovlev (2014) that is implemented in WINNET and that of SKYNET (Lippuner & Roberts 2017), which uses a parameterization of Dewitt et al. (1973) are shown in Figure 2. In the most relevant regime for nucleosynthesis calculations (i.e., $1 \lesssim \Gamma_{12} \lesssim 200$), all schemes show good agreement (Figure 2). For higher values of $\Gamma_{12} > 200$, the temperature is usually close to or even below the validity of the reaction rate

databases (see $T_{\min} = 10^{-2}$ GK of the Reaclib reaction rate database; Cyburt et al. 2010).

Screening corrections will modify the reaction rates according to

$$\langle \sigma v \rangle_{\mathrm{scr}} = \langle \sigma v \rangle f_{\mathrm{scr}}. \qquad (45)$$

The implementation of screening with more than two reactants is realized in several steps. For three reactants, the screening correction of only two reactants is calculated, and, in a next step, the correction of the third reactant with the summed mass and ion number of the first two reactants is calculated. This corresponds to forming a short-lived intermediate nucleus. The total correction is then given by the multiplication of both correction factors f_{scr}.

In the case of NSE (see Section 2.3), screening corrections enter in the form of a change of the binding energy of a charged nucleus, i.e., the difference in the Helmholtz free energy due to the screening. Since all reactions are in equilibrium, we can assume that every nucleus is built by a series of proton captures and neutron captures, where the latter reaction is independent of screening corrections. To obtain a correction for the binding energy of a given nucleus with charge number Z, we therefore multiply the screening corrections f_{scr} of the necessary amount of $(Z - 1)$ proton captures.[21] The impact of screening and the consistency of the network at NSE transition is shown in Figure 1. Note that other approaches exist that derive the screening corrections from the detailed balance principle (e.g., Kushnir et al. 2019) or from a global Coulomb correction (Bravo & García-Senz 1999; Lippuner & Roberts 2017). All of these approaches are consistent with each other. When taking screening corrections into account, heavier nuclei are synthesized compared to the case without screening.
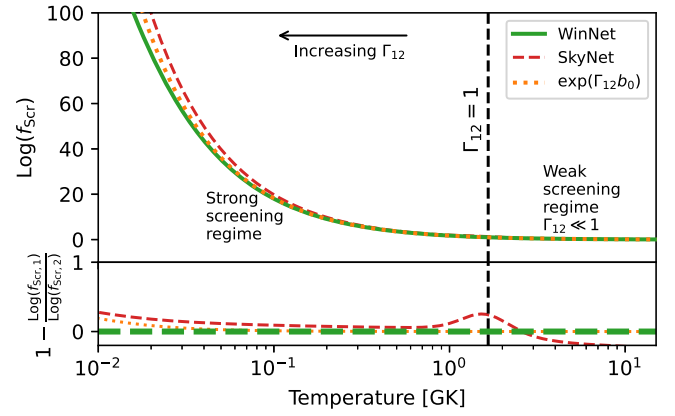
3. Methods and Numerical Techniques

3.1. Code Structure and Flow Diagram

In the following, we describe the control flow of WINNET (see Figure 3). The code starts by reading a user-defined file in the initialization step. This file contains runtime parameters such as paths to nuclear physics input data and other options. A full list of possible parameters is given in the documentation of the code.

After the initialization, the evolution mode is chosen. This mode is set to either "Network" or "NSE" and depends on the temperature. The implementation of several modes is necessary as the most efficient approach to determine the composition changes with temperature. Whereas solving the full network equations in a temperature regime where an equilibrium holds can lead to arbitrarily small time steps, solving NSE conditions at too low temperatures can lead to incorrect results.

For both evolution modes, the temperature, density, and neutrino quantities (i.e., neutrino temperatures or energies and luminosities) are updated using either an interpolation (i.e., linear, cubic, Akima, modified Akima, Pchip) within the thermodynamic data of the Lagrangian tracer particle, analytic equations, or a user-defined extrapolation (i.e., adiabatic, exponential, free). In the network regime, updating the temperature depends on the input settings and includes some special cases. If the user allows feedback of the nuclear energy

---
[21] Note that XNet uses the same approach in NSE; see https://github.com/starkiller-astro/XNet/blob/master/doc/screening/Screening_for_NSE.pdf.

Figure 2. Upper panel: screening correction for the heavy ion reaction $^{12}\mathrm{C} + ^{12}\mathrm{C}$ for a constant density of 10^8 g cm^{-3} and $Y_e = 0.5$. The screening correction of Kravchuk & Yakovlev (2014) that is used in WINNET is shown as the solid green line. The screening correction of Kravchuk & Yakovlev (2014) when only using the b_0 term that is similar to the original description of Salpeter (1954) is shown as the dotted orange line. The screening correction of SKYNET for a pure carbon composition is shown as the dashed red line. Bottom panel: relative differences of the screening corrections relative to that implemented in WINNET. The vertical dashed line indicates the intermediate screening regime for $\Gamma_{12} = 1$.

release on the temperature, a differential equation of the entropy is solved explicitly together with the nuclear reaction network equations (see Section 2.4). After updating the temperature, density, and neutrino properties, the reaction network equations are solved numerically. For the network regime, the full set of coupled differential equations (including all reactions) is solved. In NSE, Equations (23), (24), and (25) are solved for a given temperature, density, and electron fraction. The latter is evolved taking weak reactions into account only.

If no convergence is achieved (the criteria are introduced in Section 3.2), the step size is halved, and the iteration is repeated. Otherwise, an output is generated, and the time is evolved (indicated by "rotate timelevels" in Figure 3). The main loop ends when a user-defined termination criterion is fulfilled. Before the code terminates, final output such as the final abundances and mass fractions are written.

3.2. Integration Schemes

Due to the stiff behavior of the nuclear reaction network equations (Equation (20)), implicit/backwards methods are necessary to integrate the ODE. The general structure of the network however is independent of the chosen integration method.

Regardless of the chosen integration method, WINNET uses a sparse matrix representation of the Jacobian of the system and the sparse matrix solver PARDISO (Schenk & Gärtner 2004), which is OpenMP parallelized. For a detailed description of the sparse format, see, e.g., Hix & Thielemann (1999) or Winteler (2012). This sparse format brings a computational advantage for calculations with more than $N \gtrsim 400$ nuclei. In WINNET, the indices of possible nonvanishing entries are calculated once at the beginning and are updated in a next step when solving the linear system. WINNET provides two methods to integrate the system that are outlined subsequently.

3.2.1. Implicit Euler

The implicit Euler method (see also, e.g., Hix & Thielemann 1999; Winteler 2012; Lippuner & Roberts 2017) is one of the
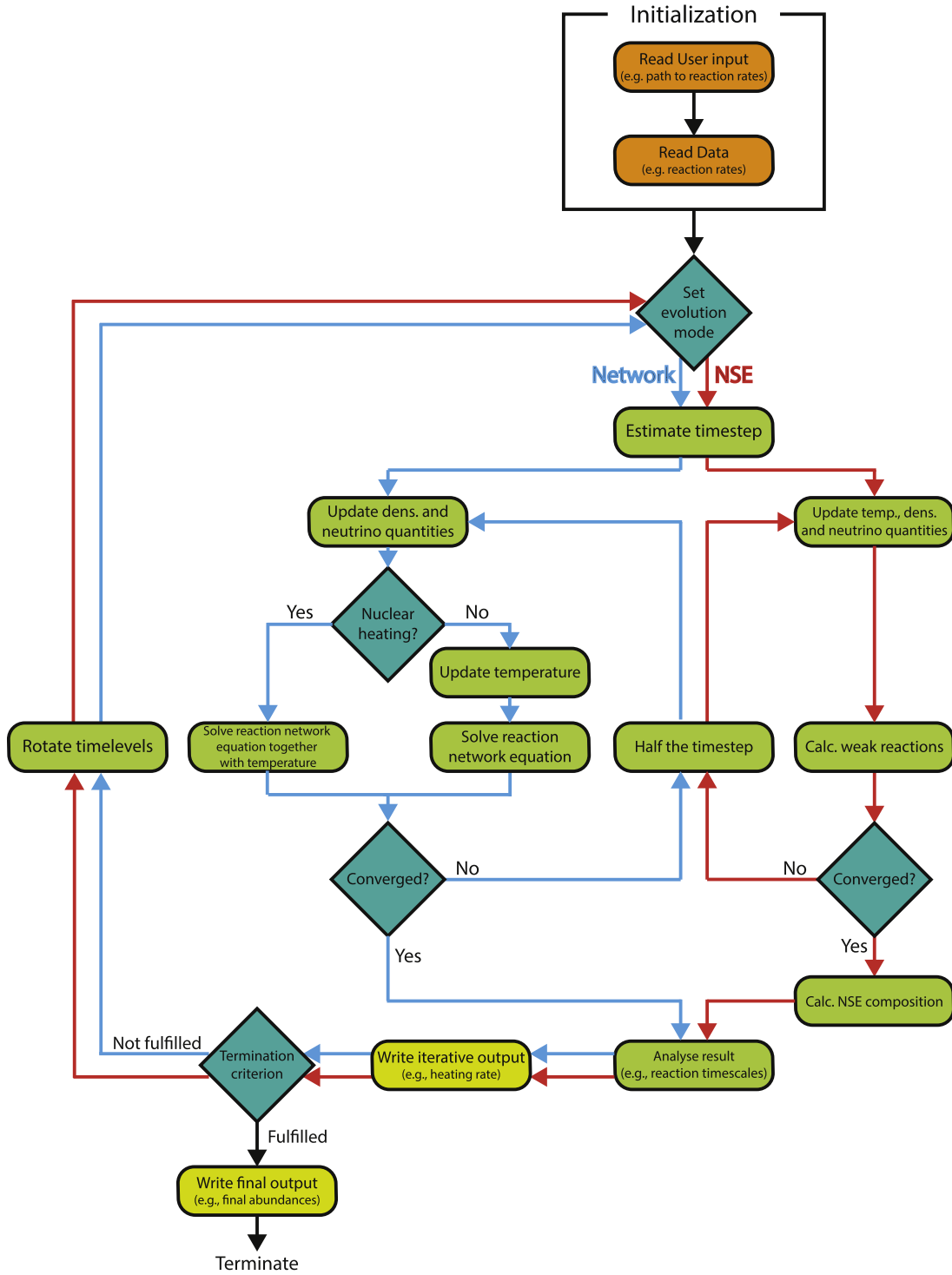
Figure 3. Flow diagram of WINNET. Figure taken from Reichert (2021).

simplest implicit integration methods. Nevertheless, it is sufficient for most of the calculations, especially when a large number of nuclei is involved in the calculation. For a coupled ODE, we can formulate the problem of integrating the equation by the general form of

$$\frac{DY_i}{Dt} = \dot{Y}_i = f_i(t, Y_1, \ldots, Y_N),$$ (46)

where N is the number of involved species, and Y_i is the abundance of species i. There are two possibilities to discretize

this derivative. The simplest approach would be

$$\frac{Y_i(t + h) - Y_i(t)}{h} = f_i(t, Y_1, \ldots, Y_N).$$ (47)

When choosing a time step h, everything except $Y_i(t + h)$ is known, and one can integrate the ODE when knowing an initial value of Y_i. However, this approach corresponds to an explicit Euler method, an integration scheme that can be numerically unstable for so-called stiff problems that are present in reaction

networks. Therefore, we can discretize the derivative with

$$\frac{Y_i(t + h) - Y_i(t)}{h} = f_i(t + h, Y_1,...,Y_N). \qquad (48)$$

Note that here $Y_i(t + h)$ as well as $f_i(t + h, Y_1,...,Y_N)$ is unknown. We can derive a iterative formula for the solution of $Y_i(t + h)$. This is given by:

$$Y_i(t + h) = Y_i(t) + h f_i(t + h, Y_1,...,Y_N). \qquad (49)$$

To get a solution, we have to apply a root-finding algorithm; in WINNET we use the Newton–Raphson method. To apply the Newton–Raphson method, we must reformulate the problem:

$$0 = Y_i(t) + h f_i(t + h, Y_1,...,Y_N) - Y_i(t + h). \qquad (50)$$

Mathematically, a multidimensional Newton–Raphson can be formulated as

$$\boldsymbol{F}(\boldsymbol{x}) = 0, \qquad (51)$$

which we will later apply and set $\boldsymbol{x}$ to $\boldsymbol{Y}$. The Taylor series of $\boldsymbol{F}$ can be expressed in first order as

$$F_i(\boldsymbol{x} + \delta\boldsymbol{x}) = F_i(\boldsymbol{x}) + \sum_{j=1}^{N} \frac{\partial F_i}{\partial x_j} \delta x_j + O(\delta\boldsymbol{x}^2) = 0, \qquad (52)$$

where $\frac{\partial F_i}{\partial x_j}$ is one entry of the Jacobian matrix containing the partial derivatives of $\boldsymbol{F}$, defined as $J_{ij} = \frac{\partial F_i}{\partial x_j}$. Within WINNET, this Jacobian is represented in a sparse format. The position of zero entries is reevaluated in every iteration. Furthermore, derivatives of the screening correction factor (Section 2.5) are considered to be zero, and we calculate the Jacobian analytically as, in this case, it is just the derivative of a polynomial equation (Equation (20)). To find the root of $\boldsymbol{F}$, we iterate

$$\boldsymbol{x}^{k+1} = \boldsymbol{x}^k + \delta\boldsymbol{x}^k = \boldsymbol{x}^k - J(\boldsymbol{x}^k)^{-1} \cdot \boldsymbol{F}(\boldsymbol{x}^k) \qquad (53)$$

until convergence is reached. In a classical Newton–Raphson, the convergence criterion is given by $|\boldsymbol{x}^{k+1} - \boldsymbol{x}^k| < \epsilon_{NR}$. In WINNET we implemented a different criterion that is based on mass conservation by using the mass fraction X_i (see Equation (24)):

$$\sum_{i=1}^{N} Y_i A_i - 1 = \sum_{i=1}^{N} X_i - 1 < \epsilon_{NR} \qquad (54)$$

where $\epsilon_{NR} < 10^{-5}$ is used per default in WINNET. As investigated by Lippuner & Roberts (2017), this convergence criterion is sufficient for most of the nucleosynthesis calculations. Other convergence criteria such as $|\boldsymbol{x}^{k+1} - \boldsymbol{x}^k| < \epsilon_{NR}$ are often too strict and slow down the calculation significantly. If the Newton–Raphson does not converge, the calculation is repeated with a halved time step. This is schematically shown by the loop in Figure 3. In the case of nuclear heating being enabled (Section 2.4), the temperature change relative to the last Newton–Raphson iteration can also be limited in order to assure the convergence of the entropy update. We tested the convergence in more detail in the Appendix. By combining

Equations (53) and (49), we obtain

$$\boldsymbol{Y}_{n+1}^{k+1} = \boldsymbol{Y}_{n+1}^k - \left(\frac{1}{h} \times \boldsymbol{1} - \frac{\partial f (\boldsymbol{Y}_{n+1}^k)}{\partial \boldsymbol{Y}_{n+1}^k} \right)^{-1} \cdot \left(\frac{\boldsymbol{Y}_{n+1}^k - \boldsymbol{Y}_n}{h} - \boldsymbol{f}(\boldsymbol{Y}_{n+1}^k) \right). \qquad (55)$$

Compared to other numerical integration methods, within the implicit Euler method no intrinsic error estimation is possible. Multistep algorithms exist that calculate an integration error by comparing the result of the integration after a full time step with the result after two half steps. This however increases the computational cost, and we therefore only estimated the error based on a maximum change of the abundances ϵ_{Euler}, which is based on the current derivative. We note that this procedure is similar to the time-step estimate of SKYNET (Lippuner & Roberts 2017). The approximate change within one time step is calculated by

$$|\dot{\boldsymbol{Y}}(t)| = \left| \frac{\boldsymbol{Y}(t + h') - \boldsymbol{Y}(t)}{h'} \right| \qquad (56)$$

$$\epsilon_{Euler} = \max \left| 1 - \frac{\boldsymbol{Y}(t + h')}{\boldsymbol{Y}(t)} \right|; \qquad (57)$$

therefore, we obtain

$$|\dot{\boldsymbol{Y}}(t)| = \left| \frac{(1 - \epsilon_{Euler})\boldsymbol{Y}(t) - \boldsymbol{Y}(t)}{h'} \right| \Rightarrow h' = \epsilon_{Euler} \max \left| \frac{\boldsymbol{Y}(t)}{\dot{\boldsymbol{Y}}(t)} \right|. \qquad (58)$$

The default value in WINNET for ϵ_{Euler} is set to a maximum change of 10%. In order to avoid rapid changes of the time step, it is limited by the previous step size

$$h' = \min \left(C h, \epsilon_{Euler} \max \left| \frac{\boldsymbol{Y}(t)}{\dot{\boldsymbol{Y}}(t)} \right| \right) \qquad (59)$$

with the constant $C > 1$. Furthermore, only species with abundances higher than a threshold abundance are taken into account in the time-step calculation (default in WINNET is 10^{-10}). Additionally, the step size is restricted to a maximum change of the density within one time step (default value 5%) in order to get an adequate resolution for large density gradients. In case that nuclear heating is not enabled, the same restriction is applied to the temperature.

3.2.2. Gear's Method

In contrast to Euler's method, Gear's method (Gear 1971, see also, e.g., Byrne & Hindmarsh 1975; Longland et al. 2014; Martin 2017) includes terms of higher orders (see also Timmes 1999, for a discussion of the advantages of higher-order solvers for nuclear reaction networks). In the following, we will denote the highest included order with q. It is a so-called predictor–corrector method, where in a first step, a rough solution is guessed, and in a second step, this solution is corrected until a given precision is reached. The first prediction is based on information of the past behavior of the system. Therefore, the so-called Nordsieck vector

$$\boldsymbol{z}_n = \left(\boldsymbol{Y}_n, h\dot{\boldsymbol{Y}}_n, \frac{h^2 \ddot{\boldsymbol{Y}}_n}{2!},..., \frac{h^q \boldsymbol{Y}_n^{(q)}}{q!} \right) \qquad (60)$$

is stored, where Y_n are the abundances at the current time, $\dot{Y}_n$, $\ddot{Y}_n$,...,$Y_n^{(q)}$ are the time derivatives of the abundances, and $h = t_{n+1} - t_n$ is the current step size. In order to obtain the predictor step $z_{n+1}^{(0)}$, the Nordsieck vector is multiplied by a $(q+1) \times (q+1)$ Pascal triangle matrix defined by

$$A^{ij}(q) = \begin{cases} 0 & \text{if } i < j \\ \binom{i}{j} = \frac{i!}{j!(i-j)!} & \text{if } i \geqslant j \end{cases} \quad \text{with } i, j \in [0, 1,...,q].$$

(61)

Therefore, the predictor step is given by

$$z_{n+1}^{(0)} = z_n \cdot A,$$

(62)

which is the Taylor series of Y_n truncated at the order of q in matrix notation. To obtain an accurate solution for Y_{n+1}, the predictor step is iteratively corrected due to

$$z_{n+1} = z_{n+1}^{(0)} + e_{n+1} \cdot \ell,$$

(63)

with the correction vector e_{n+1}. ℓ is a $1 \times (q+1)$ vector given by

$$\sum_{j=0}^{q} \ell_j x^j = \prod_{i=1}^{q} \left(1 + \frac{(t - t_{n+1})/h}{(t_{n+1} - t_{n+1-i})/h}\right) = \prod_{i=1}^{q} \left(1 + \frac{x}{\xi_i}\right).$$

(64)

Here, we defined the vector ξ storing the information of previous step sizes. The components of $\ell = [\ell_0(q), \ell_1(q),...,\ell_j(q),...,\ell_q(q)]$ are calculated as

$$\ell_0(q) = 1,$$
$$\ell_1(q) = \sum_{i=1}^{q} (\xi_i^{-1}),$$
$$\ell_j(q) = \ell_j(q-1) + \ell_{j-1}(q-1)/\xi_q,$$
$$\ell_q(q) = \left(\prod_{i=1}^{q} \xi_i\right)^{-1}.$$

(65)

The correction vector e_n is calculated using the same Newton–Raphson scheme as for the solution Y_{n+1}. To obtain the composition of the next step,

$$\left[1 - \frac{h}{\ell_1}J\right]\Delta^{(m)} = -(Y_{n+1}^{(m)} - Y_{n+1}^{(0)}) + \frac{h}{\ell_1}(\dot{Y}_{n+1}^{(m)} - \dot{Y}_{n+1}^{(0)}),$$
$$Y_{n+1}^{(m+1)} = Y_{n+1}^{(m)} + \Delta^{(m)}$$

(66)

is solved. Here, $Y_{n+1}^{(0)}$ and $\dot{Y}_{n+1}^{(0)}$ are extracted from the first and second entry of $z_{n+1}^{(0)}$. The index m is the number of iterations, $\Delta^{(m)}$ is an iterative correction, and J is the Jacobian matrix

$$J_{ij} = \frac{\partial \dot{Y}_{i,n+1}^{(m)}}{\partial Y_{j,n+1}^{(m)}}.$$

(67)

Identically to the implicit Euler integration, the Jacobian is represented by a sparse matrix, for which zero entries are evaluated in every step. Calculating the Jacobian is one of the most expensive steps when solving the ODE. Therefore, some integration packages use so-called 'Jacobian caching' to tackle the problem of recalculating the Jacobian multiple times (e.g.,

VODE; Brown et al. 1989). We investigated a similar technique, Broyden's method (Broyden 1965), to approximate the Jacobian instead of recalculating it in every iteration. This, however, did not lead to a performance improvement due to rapid changes of the reaction rates and feedback from the nuclear reactions on the temperature. Therefore, more Newton–Raphson iterations were needed to obtain convergence leading to an overall performance loss. After the Newton–Raphson iteration has converged, the correction vector

$$e_{n+1} = Y_{n+1} - Y_{n+1}^{(0)}$$

(68)

can be determined. To obtain a sophisticated guess of the time step within a given tolerance, the error can be estimated by the truncation error

$$E_{n+1}(q) = -\frac{1}{\ell_1}\left[1 + \prod_{i=2}^{q}\left(\frac{t_{n+1} - t_{n+1-i}}{t_n - t_{n+1-i}}\right)\right]^{-1} e_{n+1}.$$

(69)

The next time step is computed within a certain allowed tolerance ϵ_{Gear} by

$$h' = hK\left(\frac{\epsilon_{\text{Gear}}}{\max \bar{E}_{n+1}(q)}\right)^{1/q+1},$$

(70)

where K is a conservative factor usually chosen in the interval $K \in [0.1, 0.4]$. As for the calculation of the step size in Equation (59), only abundances above a certain threshold should contribute to the calculation of the new time step. Therefore, the truncation error is rescaled in order to prevent an overweighting of the change of very small abundances, smaller than a threshold Y_{limit} (default in WINNET: 10^{-10}),

$$\bar{E}_{i,n+1} = \begin{cases} E_{i,n+1}/Y_i & \text{if } Y_i > Y_{\text{limit}} \\ E_{i,n+1}/Y_{\text{limit}} & \text{if } Y_i \leqslant Y_{\text{limit}} \end{cases}.$$

(71)

In addition to the automatic control of the step size, the order q can be selected automatically as well. For this, we allow only order changes of $q \pm 1$. The error estimates for increasing and decreasing order are calculated by

$$E_{n+1}(q-1) = -\frac{\prod_{i=1}^{q-1} \xi_i}{\ell_1(q-1)} \frac{h^q Y_{n+1}^{(q)}}{q!}$$

(72)

$$E_{n+1}(q+1) = \frac{-\xi_{q+1}(e_{n+1} - Q_{n+1}e_n)}{(q+2)\ell_1(q+1)\left[1 + \prod_{i=2}^{q} \frac{t_{n+1} - t_{n+1-i}}{t_n - t_{n+1-i}}\right]},$$

(73)

where Q and C are defined as

$$Q_{n+1} = \frac{C_{n+1}}{C_n}\left(\frac{h_{n+1}}{h_n}\right)^{q+1}$$

(74)

$$C_{n+1} = \frac{\prod_{i=1}^{q} \xi_i}{(q+1)!}\left[1 + \prod_{i=2}^{q} \frac{t_{n+1} - t_{n+1-i}}{t_n - t_{n+1-i}}\right].$$

(75)

To obtain the most efficient way of calculating the solution of the ODE, the step size in Equation (70) is calculated for order $q - 1$, q, and $q + 1$, respectively. The order is chosen as the one providing

the largest time step, $h' = \max(h'(q-1), h'(q), h'(q+1))$. Since the Nordsieck vector depends on the step size (see Equation (60)), it must be rescaled whenever the step size is changed:

$$z'_{n+1} = \mathrm{diag}(1, \eta, \eta^2, \ldots, \eta^q) \cdot z_{n+1}, \qquad (76)$$

where $\eta = h'/h$. Also, when the order decreases to $q-1$, the Nordsieck vector has to be rescaled. Therefore, we define a correction

$$\Delta'_i = d_i z_{q,n+1}, \qquad (77)$$

where, similar to Equation (64), d is implicitly defined as

$$\sum_{j=0}^{q} d_j x^j = x^2 \prod_{i=1}^{q-2} (x + \xi_i), \qquad (78)$$

and its components are given by

$$d_0(q) = d_1(q) = 0$$
$$d_2(q) = \prod_{i=1}^{q-2} \xi_i,$$
$$d_j(q) = \xi_{q-2} d_j(q-1) + d_{j-1}(q-1),$$
$$d_{q-1}(q) = \sum_{i=1}^{q-2} \xi_i,$$
$$d_q(q) = 1.$$

Due to the implementation of higher orders, within Gear's method, one is able to apply larger step sizes compared to the implicit Euler scheme, reducing the amount of iterations drastically without losing accuracy. However, for most of the calculations, more Newton–Raphson iterations are necessary, resulting in similar or even higher computational costs. The difference between the implicit Euler and Gears method is discussed in more detail in the Appendix.

4. Reaction Network Inputs

4.1. Lagrangian Tracer Particles

The nuclear reaction network equations (Equation (20)) contain a dependency on the temperature and density of the environment. To get an initial composition from NSE, additionally the electron fraction is necessary. These quantities have therefore to be recorded from a simulation of an astrophysical scenario. This is often done in terms of Lagrangian tracer particles within the hydrodynamic simulation. These particles (also called *trajectories* or *tracer*) are passively advected within the (M)HD simulation, tracing all relevant quantities such as the time, temperature, density, electron fraction, and neutrino properties. WINNET is a so-called single-zone code, i.e., tracer particles cannot interact among one another. This assumption is valid if the nuclear burning timescales are much faster than other timescales changing the abundances (e.g., diffusion). Therefore, for the majority of explosive environments we can use a single-zone reaction network; however, for some cases such as hydrostatic oxygen burning, it has to be taken with care (Hix & Thielemann 1999). There have been several studies on the uncertainties of a tracer particle method. The necessary amount of tracer particles to achieve convergence has been studied, e.g., in Seitenzahl et al. (2010) and Nishimura et al. (2015).
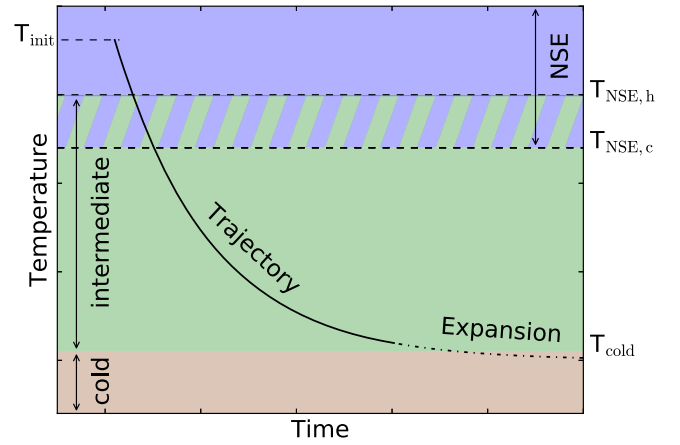

Figure 4. Sketch of different temperature regimes included in WinNet.

Also, the initial placement of the tracer particles can have an impact on the convergence of the result (Bovard & Rezzolla 2017). A detailed comparison between setting tracers in contrast to calculating the nucleosynthesis inside the hydrodynamical simulation has been presented in the context of core-collapse supernovae (CCSNe) by Harris et al. (2017) and by Navó et al. (2023). Additionally, Sieverding et al. (2023) studied the impact of obtaining tracers in a postprocessing step after the calculation of a hydrodynamic model from simulation snapshots.

4.1.1. Temperature and Density Regimes

During its evolution, a tracer particle can undergo different temperature regimes, and therefore different approaches are required to obtain the composition within the given time step. In WINNET, there are distinctions between three temperature regimes, the regime of NSE, the intermediate temperature regime, and the cold temperature regime, schematically shown in Figure 4.

In the regime of NSE, the network equations are only solved for weak reactions. Instead of calculating also strong reactions, an equilibrium is assumed (Section 2.3). When the conditions are below a certain temperature threshold T_{NSE}, the nuclear reaction network is solved for all nuclear reactions. The transition temperature between these regimes can be chosen individually, depending on whether the transition occurs from hot to intermediate temperatures ($T_{\mathrm{NSE,c}}$) or from intermediate to hot temperatures ($T_{\mathrm{NSE,h}}$, see Figure 4). The exact temperatures of the transitions depend on the environment (e.g., Khokhlov 1991). The reason for having two transition temperatures is mainly motivated when using a feedback of the nuclear energy on the temperature (Section 2.4). In this case, a slight inconsistency at the interface between the hot and intermediate regime (see Section 2.2) may cause fluctuations in the temperature that can lead to an infinitesimal time step when using only one transition temperature.

When the temperature drops below $T = 10^{-2}$ GK, all reaction rates are frozen to the lower validity limit of the JINA Reaclib reactions (brown region in Figure 4; Cyburt et al. 2010). Often, the Lagrangian tracer particle finishes before the nucleosynthesis is completed and an extrapolation of the thermodynamic conditions is required (dotted line in Figure 4). The details of these assumptions can have an impact on the final yields (see also Harris et al. 2017) and should be chosen according to the environment, e.g., a homologous expansion
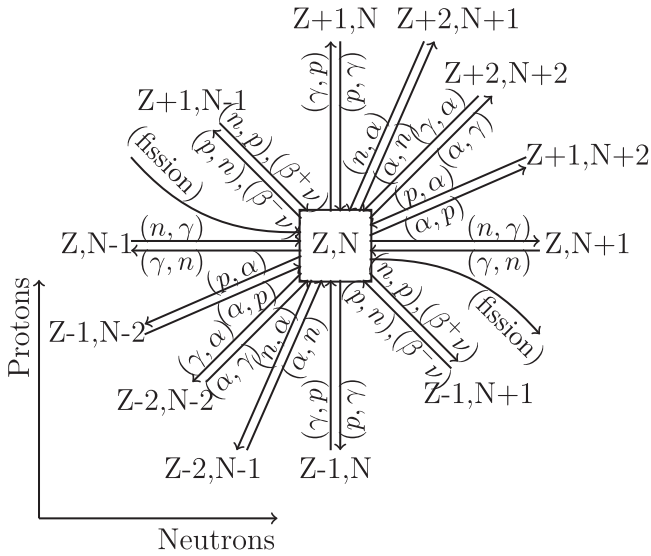
Figure 5. Sketch of the most important nuclear reactions (Reichert 2021).

for CCSNe or a free expansion for the dynamical ejecta of a neutron star merger (NSM).

4.2. Reaction Rates

Although all nuclei are connected to each other by nuclear reactions, in practice most of the reactions are negligible. The most important reactions for astrophysical environments are given by reactions that involve nucleons or α-particles, decays, neutrino reactions, electron and positron captures, or fission reactions (Figure 5). Many formats of the reaction rates exist. WINNET is built around the Reaclib reaction rate library, and this library usually contains the majority of reactions (Cyburt et al. 2010). However, other formats are also supported, e.g., tabulated reaction rates from the TALYS code (Koning et al. 2019). Rates given in different formats are either added or merged into the list of all rates within WINNET. In this case, the different formats have different priorities, starting with the Reaclib reactions with the lowest priority. If, in addition, this rate is also included in the theoretical β^+, β^-, electron-capture, and positron-capture rates, it is replaced once again. The priority of the individual rates is shown in Figure 6.

We note that WINNET does not perform any evaluation on the reliability of a rate. If a rate is contained multiple times in different formats,[22] it is the user's responsibility to choose the desired rate by either fully automatically using the one with the highest priority as in Figure 6 or by deleting unwanted rates from high-priority formats. The modular structure of WINNET allows for an easy implementation of other popular reaction rate formats. In the following, we give a short overview of the current supported file formats.

4.2.1. Reaclib File Format

Most of the nuclear reaction rates are given in form of seven fit parameters, a_i, the so-called Reaclib[23] format

---

[22] Not to confuse with a rate being contained multiple times in the same format, which can happen due to, e.g., resonances in the rate.
[23] See https://reaclib.jinaweb.org/index.php and Rauscher & Thielemann (2000) and Thielemann (1980) for more details about the format and for recent reaction rates.
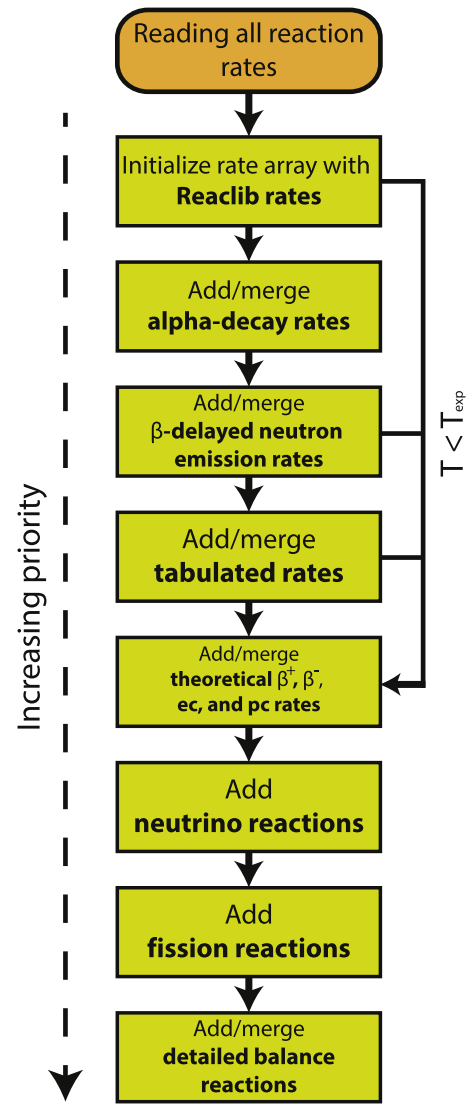
Figure 6. Sketch of the rate replacement procedure. Reaction rates in different formats have different priorities when creating a list with all reactions within WINNET. The priority of the rates increases from the top to the bottom of the plot. At a certain threshold temperature T_{exp}, theoretical β^+, β^-, ec, and pc rates get replaced again as they are only valid above certain temperatures (see the text). With the exception of Reaclib rates, all other rates are only optionally used.

(Cyburt et al. 2010). The reaction rate is calculated according to:

$$R = \exp\left[a_0 + \sum_{i=1}^{5} a_i T_9^{\frac{2i-5}{3}} + a_6 \ln T_9\right]. \qquad (79)$$

Depending on the reaction, R can be either λ, $N_A\langle\sigma\rangle_{i,j}$, or $N_A^2\langle ijk\rangle$ (see Equation (20)). Reverse reactions have additionally to be multiplied by the partition functions (see the pre-factor in Equation (21)) that are also provided within the Reaclib database in a separate file (with the data originating from Rauscher & Thielemann (2000) and Cyburt et al. (2010) for more proton-rich nuclei). For higher temperatures ($T > 10$ GK), partition functions from Rauscher (2003) can be used. The fits of the reaction rates are valid between 10^{-2} GK $\leqslant T \leqslant 10^2$ GK. For lower temperatures, within WINNET, the rates are kept constant. At higher temperatures,

Table 1
Numbers of Reactants and Products for Different Reaclib Chapters

Chapter	No. Reactants	No. Products
1	1	1
2	1	2
3	1	3
4	2	1
5	2	2
6	2	3
7	2	4
8	3	1
9	3	2
10	4	2
11	1	4

usually NSE is assumed that only depends on the binding energies and partition functions.

Each reaction belongs to a specific chapter in the Reaclib tables as given in Table 1. The Reaclib chapters correspond to different one-, two-, and three-body terms in Equation (20), where each of these terms in the summation can include different numbers of reaction products. Another Reaclib format includes Chapters 8 and 9 together and does not include Chapters 10 and 11. WINNET supports and automatically detects both options. We note that the Reaclib reactions also contain two isomers of ^{26}Al. WINNET can take these isomers into account when adding their properties into the winvn and in the list of considered nuclei. They will then be treated like all other nuclei.

4.2.2. Parametric α Decays

The Reaclib reaction rate database contains only experimental α decays. To make the α decays more complete, WINNET is able to calculate additional α decays with the Viola-Seaborg formula (e.g., Viola & Seaborg 1966; Sobiczewski & Patyk 1989; Brown 1992; Sahu & Bhoi 2016). We provide rate tables of α decays using the parameterization of Dong & Ren (2005). For $Z > 84$ and $N > 126$, they fitted experimentally determined α decays with

$$\log_{10} T_\alpha = (aZ + b)Q_\alpha^{-0.5} + (cZ + d) + h_{\log}, \quad (80)$$

where Z is the proton number of the decaying nucleus, Q_α is the Q-value of the decay, and the parameters $a = 1.64062$, $b = -8.54399$, $c = -0.19430$, and $d = -33.9054$ were derived through least-squares fitting. Additionally, the so-called hindrance factor $h_{\log}$ was fitted:

$$h_{\log} = \begin{cases} 0, & Z_{\text{even}}, N_{\text{even}} \\ 0.8937, & Z_{\text{even}}, N_{\text{odd}} \\ 0.5720, & Z_{\text{odd}}, N_{\text{even}} \\ 0.9380, & Z_{\text{odd}}, N_{\text{odd}} \end{cases}. \quad (81)$$

An obvious consequence of this parameterization is that α decays happen on shorter timescales if Q_α is large or, in other words, they are more relevant for regions with high Q_α (see upper and middle panels of Figure 7). It has been pointed out that this fit is only valid for their fitting regions; other regions need a separate fit. To also obtain a valid fit to the other regions, we use the masses and experimental α-decay half-lives of the Reaclib. We therefore use the above parameters only for
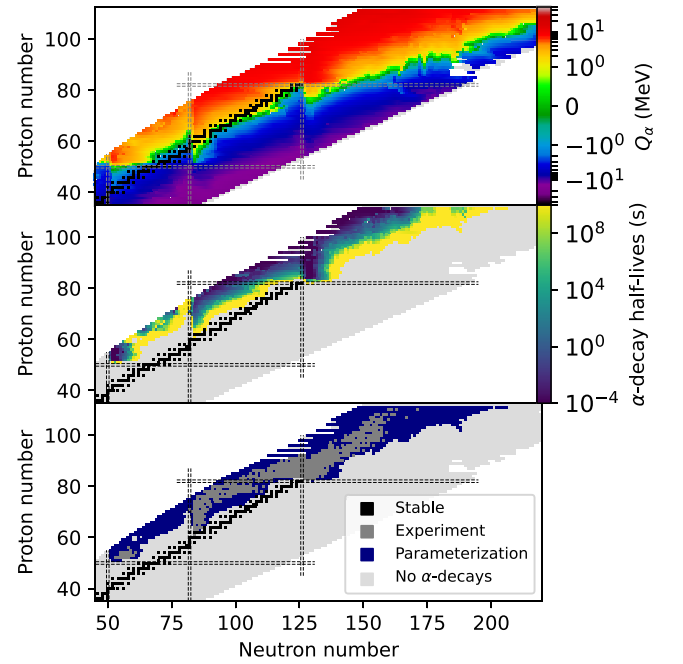

Figure 7. Upper panel: Q-value for α decay using the masses provided with the Jina Reaclib. Second panel: α-decay half-lives in seconds. Whenever experimental α-decay half-lives are available, we plot these instead of the parameterized ones. Nuclei that have half-lives of $T_{1/2} \gtrsim 10^{12}$ yr are assumed to not α decay. Bottom panel: distinction between parameterized and experimentally known α-decay half-lives included in the Jina Reaclib. Stable nuclei are shown as black squares, experimentally available α decays within the Jina Reaclib are indicated as dark-gray rectangles. Magic numbers of 50, 82, and 126 are shown as dashed lines. All shown rates are publicly available along with WINNET.

nuclei with $Z \geqslant 82$ and $N \geqslant 126$, while we use the parameters of Table 2 for the other regions.

This fit over these four individual regions of the nuclear chart that correspond to the regions between magic numbers is in a much better agreement to the experimental half-lives (Figure 8). Still, some deviations of around 1–2 magnitudes are present around the magic numbers. When comparing all available experimental α decays with the calculated ones, we obtain a standard deviation of $\sigma_{Z\text{even},N\text{even}} = 0.38$, $\sigma_{Z\text{odd},N\text{even}} = 1.61$, $\sigma_{Z\text{even},N\text{odd}} = 0.93$, and $\sigma_{Z\text{odd},N\text{odd}} = 0.82$. The large standard deviation of $\sigma_{Z\text{odd},N\text{even}}$ is driven by the decay of ^{153}Lu whose half-life differs by more than 16 mag (3.9×10^{16} s versus an experimental value of ~ 1.3 s). Note that ^{153}Lu has a magic neutron number of 82; nevertheless, the difference between the Viola–Seaborg formula and the experimental value is quite remarkable and indeed possibly a result of an outdated rate in the Jina Reaclib that uses the experimental data last evaluated in 2017. The latest experimental data from 2019 indicates that this nucleus is entirely decaying by an ec/β^+ decay,[24] which would agree with the large half-life obtained with our fitted formula. When removing this nucleus from the calculation of the standard deviation, it reduces to $\sigma_{Z\text{odd},N\text{even}} = 0.64$. We therefore have excluded it from our least-squares fit. The obtained half-lives are illustrated in Figure 7. The additional α decays are mostly located at the proton-rich side of the valley of stability or very heavy nuclei. They therefore impact the nucleosynthesis in very neutron-rich

---

[24] https://www-nds.iaea.org/exfor/servlet/E4sGetIntSection?SectID=14658963&req=2130
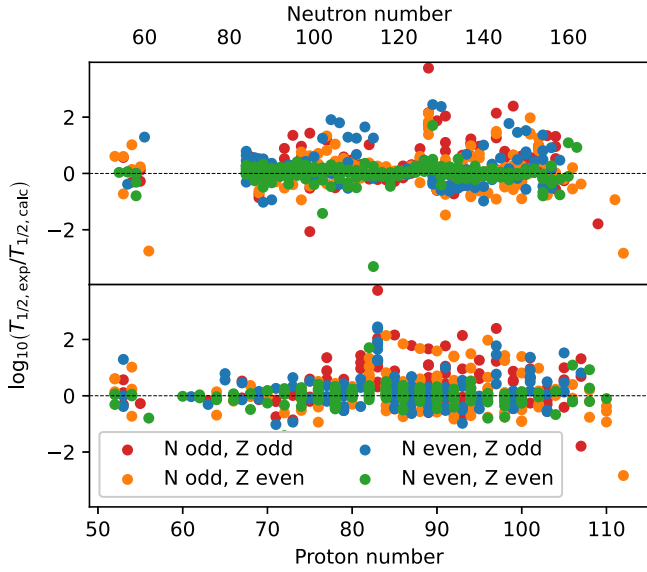
Figure 8. Ratio of calculated and experimental α-decay half-lives. The upper panel shows the ratio versus neutron number, the lower panel versus proton number. The different colors indicate the different types of nuclei as indicated in the legend.

Table 2
Fitted Parameters for Equation (80)

	a	b	c	d
$Z > 82\ N > 126$	1.64062	−8.54399	−0.19430	−33.9054
$Z > 82\ 82 < N \leqslant 126$	1.71183	−7.50481	−0.25315	−30.7028
$50 < Z \leqslant 82$ $82 < N \leqslant 126$	1.70875	−7.52265	−0.25153	−30.8245
$50 < Z \leqslant 82$ $50 < N \leqslant 82$	1.71371	−7.34226	−0.24978	−30.6826
	h1	h2	h3	h4
$Z > 82\ N > 126$	0	0.8937	0.5720	0.9380
$Z > 82\ 82 < N \leqslant 126$	0	0.0476	0.1214	0.3933
$50 < Z \leqslant 82$ $82 < N \leqslant 126$	0	0.2140	0.0600	0.4999
$50 < Z \leqslant 82$ $50 < N \leqslant 82$	0	−0.1242	1.1799	0.7166

Note. For $Z > 82$, $N > 126$, we use the parameterization of Dong & Ren (2005). The lower part of the table shows the hindrance factors, and h1 indicates Z_{even} and N_{even}, h2 Z_{even} and N_{odd}, h3 Z_{odd} and N_{even}, and h4 Z_{odd} and N_{odd}.

conditions that synthesize elements in the very heavy region or possibly during the γ- or p-process where heavier nuclei get photodisintegrated, and the nucleosynthetic flow moves along the proton-rich side. We note that one could add proton-emitters (nuclei that decay by emitting a proton without previously undergoing β decay) in a similar fashion. This decay would be most relevant for nucleosynthetic paths along the proton-dripline at low mass numbers. There are some works on predicting the half-life of this decay (e.g., Basu et al. 2005; Bhattacharya & Gangopadhyay 2007; Dong et al. 2009; Qi et al. 2012; Saxena et al. 2023). However, proton-emission is somewhat more complex to describe and depends more strongly on the Q-value as well as on often unknown properties, such as the angular momentum transfer of the decay. Furthermore, the conditions under which these reactions are relevant are quite exotic, and we therefore did not attempt to include them.

On a technical level, within WINNET, one can decide if the α-decay rates should only supplement the Reaclib rates or also replace them. The latter may become interesting in the future in case other theoretical α decays will be added to the Reaclib. In addition, one can adjust between which proton numbers' α decays are added. Within WINNET we provide a file with the α-decay rates using the parameterization presented here. For the fit as well as the rates, we used the masses of the Jina Reaclib as an input.

4.2.3. Tabulated Rates

Another possible format is given in form of a tabulation. This format is common for nuclear reaction codes such as TALYS (Koning et al. 2019). Every rate is tabulated on 30 temperature grid points from 10^{-4} to 10 GK and, identical to the Reaclib format, assigned a certain chapter as given in Table 1. Reaction rates that are given in tabulated form will replace the respective reaction rates in Reaclib format. Reverse reactions can be given in tabulated form or calculated with the theory of detailed balance within WINNET. These calculations

will replace all reverse rates that are given in the reaction rate library.

4.2.4. Neutrino Reactions

Neutrino reactions are tabulated versus the neutrino temperatures from 2.8–10 MeV on seven grid points. These reaction rates enter the nuclear reaction network as an additional term in the form of

$$\frac{DY(t)}{Dt} = \langle \sigma \rangle (t)\, F_\nu(t)\, Y(t), \qquad (82)$$

with the average neutrino cross section integrated over the normalized neutrino spectrum $\langle \sigma \rangle (t)$ that depends on the neutrino temperature $T_\nu(t)$. Furthermore, $F_\nu = L_\nu / (4\pi r^2 \langle E_\nu \rangle)$ is the neutrino number flux.

WINNET includes a tabulation where the neutrino reactions on nucleons have been calculated as described in, e.g., Burrows et al. (2006) with the weak magnetism and recoil corrections as in Horowitz (2002). Within WINNET we provide the rate table as well as a python script to calculate it. In principle the full neutrino energy distribution could be taken from the hydrodynamic simulation and an appropriate neutrino temperature can be calculated based on this. In WINNET, the average neutrino energy $\langle E_\nu \rangle$ is used interchangeably with the neutrino temperature T_ν by assuming a Fermi–Dirac distribution of the neutrino energies and a zero chemical potential of the neutrinos. For this case,

$$\langle E_\nu \rangle = \frac{\mathcal{F}_3(0)}{\mathcal{F}_2(0)} T_\nu = \frac{7\pi^4}{180\,\zeta(3)} T_\nu \approx 3.1513\, T_\nu \qquad (83)$$

holds. Here ζ is Riemann's zeta function, and $\mathcal{F}_n$ are the Fermi integrals defined as

$$\mathcal{F}_n(0) = \frac{1}{\Gamma(n)} \int_0^\infty \frac{x^n}{\exp(x) + 1} dx, \qquad (84)$$

with the gamma function $\Gamma(n) = (n+1)!$. We note that current CCSNe simulations hint toward slight deviations of the Fermi–Dirac distribution. Such a deviation can have an impact on the energy integrated neutrino cross sections that we do not take

into account with the provided tabulation (e.g., Tamborra et al. 2012; Mirizzi et al. 2016; Sieverding et al. 2019).

For neutrino reactions with heavier nuclei, WINNET is able to include neutrino interactions that are provided in a separate file. This file is taken from Sieverding et al. (2018) and includes charged-current as well as neutral-current reactions. All of these reactions contain different reaction channels allowing for the ejection of light particles such as neutrons, protons, and an alpha-particle. An overview of these cross sections is illustrated in Figure 9, where we show the cross sections summed over all reaction channels and the average amount of ejected neutrons for neutral-current reactions at $T_\nu = 5$ MeV.

Including neutrinos in the calculation requires additional information in the form of either a tabulation or a parameterization of these neutrino properties. In the case of charged-current reactions, only the properties of electron neutrinos and antineutrinos have to be provided. Neutral-current reactions need additional properties of muon and tau (anti)neutrinos. Within WINNET it is assumed that the (anti)neutrino energies (or temperatures) for muon and tau neutrinos are identical ($E_{\nu_\mu} = E_{\nu_\tau}$), and they are thus included as species x, where E_{ν_x} has to be provided. Furthermore, the summed luminosities have to be provided ($L_{\nu_x} = L_{\nu_\mu} + L_{\nu_\tau}$) for neutrinos and antineutrinos. Treating muon and tau (anti)neutrinos effectively together as described above may be sufficient, as current CCSNe simulations do not really distinguish between these neutrino flavors, and little has been done in this direction so far (however, see Bollig et al. 2017).

4.2.5. Theoretical Weak Rates

Theoretical models, e.g., shell-model calculations, are used to obtain weak rates for stellar conditions. These rates are listed on a temperature and electron density grid (e.g., Fuller et al. 1985; Oda et al. 1994; Langanke & Martínez-Pinedo 2001; Pruet & Fuller 2003; Suzuki et al. 2016). A direct tabulation of the rates, however, can lead to large interpolation errors (Fuller et al. 1985). Therefore, the rates are not tabulated directly, and instead, effective $\log ft_{\text{eff}}$ is stored. This can be converted to the actual rate via (see, e.g., Langanke & Martínez-Pinedo 2001)

$$\lambda = \ln 2 \frac{I}{ft_{\text{eff}}}. \qquad (85)$$

Here, I is the phase space integral for ground-state to ground-state transitions

$$I = \int_{\omega_0 = \max(q,1)}^{\infty} \omega^2 (q + \omega)^2 S(\omega) d\omega, \qquad (86)$$

with $q = (m_i - m_f)/m_e$ the Q-value in units of the electron mass.

$$S(\omega) = \frac{1}{\exp \frac{\omega m_e c^2 - \mu_e}{k_B T} + 1}, \qquad (87)$$

with the electron chemical potential μ_e.

We note that these theoretical reaction rates usually neglect atomic electron capture, which becomes increasingly important for lower temperatures, e.g., for ^{56}Ni. Therefore, WINNET contains the possibility of replacing all theoretical decays, electron and positron captures at low temperatures with the experimental decays provided in the Reaclib.

WINNET supports an individual grid for each reaction for the tabulation of theoretical β^- and β^+ decays, and positron- and
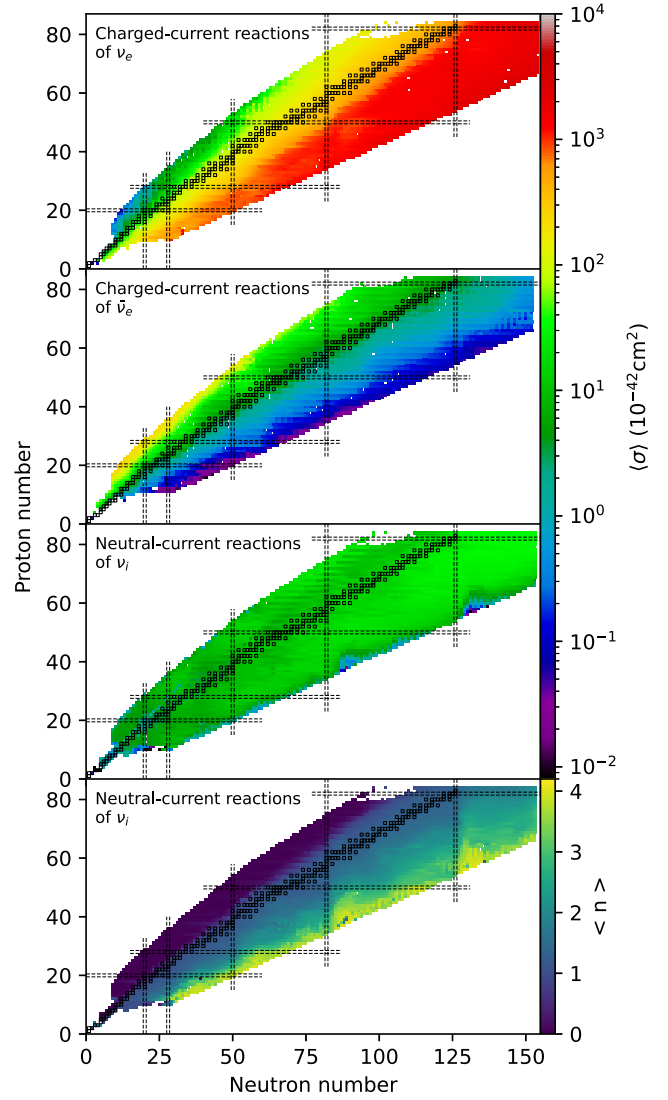

Figure 9. Energy-averaged neutrino cross sections from the table of Sieverding et al. (2018) at $T_\nu = 5$ MeV. Shown are the summed cross sections of all reaction channels. The individual panels show charged-current reactions of electron neutrinos ν_e, charged-current reactions of electron antineutrinos $\bar{\nu}_e$, neutral-current reactions of any neutrino flavor ν_i, and the average amount of neutrons for neutral-current reactions of any neutrino flavor ν_i. Note that the properties of neutral-current reactions of any antineutrino flavor $\bar{\nu}_i$ are nearly identical to the lower two panels.

electron-capture rates. This is necessary, as different available tabulations were calculated on different temperature and log ρY_e grids. We provide a table that was compiled out of various sources covering different regions of the nuclear chart (Figure 10).[25] Note that WINNET also uses electron-capture rates on protons as well as positron captures on neutrons from this table.

Since the reaction rates are tabulated with a dependence on the electron density, in principle the derivative of the reaction rate with respect to the abundances should be nonzero, and there should be a term representing this in the Jacobian of the system (Equation (52) and Equation (67)). Within WINNET we ignore this dependence and assume a zero derivative of these reaction rates.

---

[25] See https://groups.nscl.msu.edu/charge_exchange/weakrates.html.
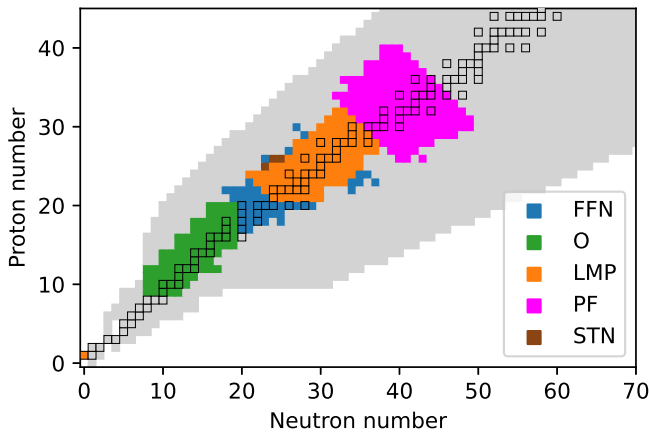
Figure 10. Compiled file of theoretical β^- and β^+ decays, and positron- and electron-capture rates, originating from different sources. The sources are FFN (Fuller et al. 1985), O (Oda et al. 1994), LMP (Langanke & Martínez-Pinedo 2001), PF (Pruet & Fuller 2003), and STN (Suzuki et al. 2016). Stable nuclei are indicated as black boxes.
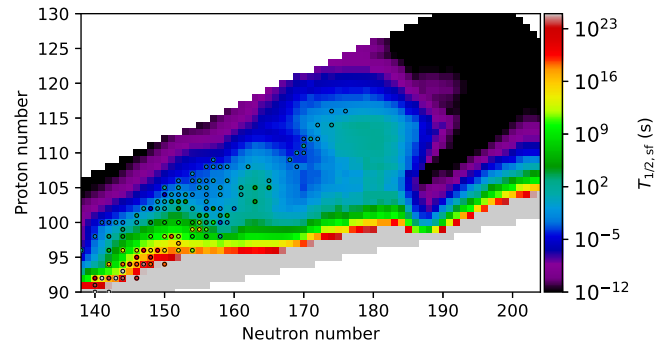
4.2.6. β-delayed Neutron Emission

The Reaclib file format only allows β-delayed neutron emissions up to three neutrons (Reaclib Chapter 11; see Table 1). In practice, decays that emit only up to two neutrons are included. The probability of all other decay channels in the Reaclib format is added to the decay channel with three products. Especially when matter far from the valley of stability on the neutron-rich side is synthesized, β-delayed neutron emission of more than two neutrons can occur (e.g., Marketin et al. 2016; Möller et al. 2019). Therefore, WINNET supports a file format containing the half-lives of the nuclei and the different channel probabilities up to the β-delayed emission of 10 neutrons. Optionally, average emitted neutrino energies can be provided in this file (to account for the energy loss when self-heating is enabled; see Section 2.4). Duplicates in Reaclib format will be replaced by the reaction rates in this format. Additionally, user-defined parameters to allow for a controlled replacement of rates exist. With them, one can specify if, e.g., experimentally measured decays should also be replaced.

4.2.7. Fission Reactions and Fragments

There are various fission modes, of which WINNET includes three: spontaneous fission, neutron-induced fission, and beta-delayed fission. In all of these cases, in addition to the probability to undergo fission, the resulting fission fragment distribution is of importance as well. Investigations for fission barrier heights utilized in astrophysics have been performed from 1980 until today (Howard & Möller 1980; Myers & Świątecki 1999; Mamdouh et al. 2001; Goriely et al. 2009; Giuliani et al. 2018a, 2018b; Vassh et al. 2019; Giuliani et al. 2020). Neutron-induced cross section predictions (or also beta-delayed fission) for astrophysical applications were treated (by, e.g., Panov et al. 2005; Martinez-Pinedo et al. 2007; Panov et al. 2010; Erler et al. 2012; Giuliani et al. 2018a). Extended compilations have been provided and can be found in several databases.[26]

In the present paper, we provide only a limited set of fission inputs, which are available within the WINNET package and are

---

[26] https://nucastro.org, https://www.jinaweb.org/science-research/scientific-resources/data and https://www-nds.iaea.org, including TALYS results.

Figure 11. Half-lives of spontaneous fission in the nuclear chart (see Khuyagbaatar 2020). Colored dots indicate experimentally measured half-lives taken from the ENDFS database.

stored in a separate file. The format is similar to the Reaclib file format, but only the name of the parent nucleus is stored. WINNET includes the rates of Panov et al. (2005) for β-delayed fission, and Panov et al. (2010) for neutron-induced fission. Reaction rates for spontaneous fission have been calculated with the semiempirical formula of Khuyagbaatar (2020), using the fission barriers provided in Möller et al. (2015). These half-lives together with experimentally measured ones are shown in Figure 11. While in Khuyagbaatar (2020) spontaneous fission half-lives were fitted to nuclei with even neutron and proton numbers only, we use the same equation for all nuclei.

The products (or fission fragments) are described by a fission fragment distribution in a probabilistic way. They can either be described by an analytic formula (Kodama & Takahashi 1975; Panov et al. 2001) or more complicated models (e.g., Kelic et al. 2009; Goriely et al. 2009; Mumpower et al. 2020). Within WINNET we include the fragment distribution of Kodama & Takahashi (1975), Panov et al. (2001), and Mumpower et al. (2020). As pointed out in Mumpower et al. (2020), the distribution should only be used for β-delayed and neutron-induced fission. Therefore, WINNET contains these fragment distributions in combination with the ones of Kodama & Takahashi (1975) for spontaneous fission.

5. Reaction Network Applications

5.1. Example Cases

In the following, we discuss several example cases calculated with WINNET that are available together with the code. These examples involve conditions of a variety of scenarios, namely the Big Bang (as described in Winteler 2012), the dynamic ejecta of an NSM (from Korobkin et al. 2012; Piran et al. 2013; Rosswog et al. 2013; Bovard et al. 2017), the neutrino-driven wind of an NSM (Perego et al. 2014; Martin et al. 2015), the viscous disk ejecta of an NSM (Wu et al. 2016; Lippuner et al. 2017), and the dynamic ejecta of a black hole neutron star merger (Korobkin et al. 2012; Piran et al. 2013; Rosswog et al. 2013). Additionally, we provide various conditions within magnetorotational supernovae (MRSNe) (Winteler et al. 2012; Obergaulinger & Aloy 2017; Aloy & Obergaulinger 2021; Obergaulinger & Aloy 2021; Reichert et al. 2021, 2023), classical novae (José & Hernanz 1998; José 2022), the X-ray burst of an accreting neutron star (Schatz et al. 2002), complete Si burning within a CCSN (with a simple parametric model as described in Nadyozhin & Deputovich 2002; Woosley et al. 2002) the neutrino-driven wind within a CCSN (Bliss et al. 2018), the detonation phase of a type Ia supernova (with a

parametric model as in Meakin et al. 2009), a main s-process (Cescutti et al. 2018; Cescutti 2022), a weak s-process (Hirschi et al. 2004; Nishimura et al. 2017a; Pignatari & Hirschi 2022), hydrostatic hydrogen burning, carbon–oxygen burning, and a simple i-process model (as described in Dardelet et al. 2015). All of these conditions are examples in WINNET and should guide the user on how to use the code. It is noteworthy that the trajectories represent typical conditions in the scenarios and may be used for sensitivity studies, but they do not necessarily reflect the total yields that can be obtained when calculating often thousands of trajectories of the individual scenarios. Further-more, a different nuclear physics input is used within the example cases, and we do not aim to exactly reproduce the abundances that have been obtained within the original publications. All example cases are very diverse in their involved conditions, and together they cover a large range of the nuclear chart. In the following sections we present only a subset of the aforementioned examples.

5.1.1. Big Bang Nucleosynthesis

The synthesis of elements during the first minutes after the origin of our Universe can be calculated with a relatively small network. Following Winteler (2012), we create a trajectory for a flat, isotropic, and homogeneous Universe to describe the conditions during the Big Bang (see also Vonlanthen et al. 2009). Furthermore, we assume a freeze-out of weak reactions at $T = 0.8$ MeV. An important quantity is the initial photon-to-baryon ratio, which was measured by the Planck satellite ($5.96 \times 10^{-10} \leqslant \eta \leqslant 6.22 \times 10^{-10}$; Planck Collaboration et al. 2016).

By creating one trajectory for each baryon-to-photon ratio, we are able to connect the Big Bang nucleosynthesis with measure-ments of abundances in stars and therefore probe the conditions of the Big Bang. For deuterium, the primordial abundance was determined to be $Y(D)/Y(H) = (2.527 \pm 0.03) \times 10^{-5}$ (Cooke et al. 2018; orange band in Figure 12). For deuterium there is a slight discrepancy with respect to the photon-to-baryon ratio determined by the Planck satellite and observed deuterium abundances. As the deuterium abundance is very sensitive to the d(p,γ)^{3}He reaction rate, this discrepancy may vanish in the future with new experimentally determined reaction rates (Mossa et al. 2020; Moscoso et al. 2021). Here, we used the rate of Descouvemont et al. (2004) that is included in the JINA Reaclib. Furthermore, observations of $Y(D)/Y(H)$ are also differing (e.g., Romano et al. 2003). The observed value of $Y(^3\mathrm{He})/Y(\mathrm{H}) = (1.1 \pm 0.2) \times 10^{-5}$ (Bania et al. 2002) is in perfect agreement with the estimated value. Additionally, the value of $Y(^4\mathrm{He}) = 1/4 \times (0.2561 \pm 0.0108)/Y(\mathrm{H})$ (Aver et al. 2010) is in agreement with our calculation (blue band in Figure 12). The observed ^{7}Li abundance ($Y(^7\mathrm{Li})/Y(\mathrm{H}) = 1.23^{+0.68}_{-0.32}$; Ryan et al. 2000) is in clear discrepancy with the calculated value. This well-known problem is referred to in the literature as the lithium problem (see, e.g., Fields 2011; Fields & Olive 2022, for reviews).

5.1.2. Main s-process

We added a trajectory of a main s-process to the example cases. This trajectory was used for a Monte Carlo sensitivity study in Cescutti et al. (2018) and can be accessed via Cescutti (2022). The trajectory was extracted from the ^{13}C pocket after the sixth thermal pulse of a solar metallicity, 3 $M_\odot$ mass AGB star (for more details, see the original publication). The final
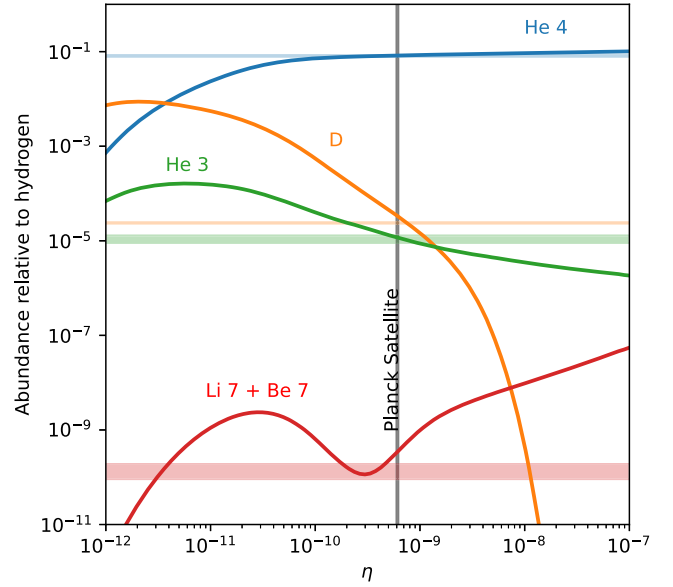
Figure 12. Final abundances relative to hydrogen as a function of the photon-to-baryon ratio η. Horizontal bands show measurements of the respective isotope.

mass fractions agree well with those of Cescutti et al. (2018; see Figure 13) given the fact that we do not attempt to use the exact same nuclear input.

5.1.3. Complete Silicon Burning

The complete Si burning can be described by analytical models. For this, we assume that the timescale behaves according to the freefall timescale (e.g., Arnett 1996):

$$\tau \approx \frac{446}{\sqrt{\rho}}. \tag{88}$$

The density ρ and the temperature T are assumed to follow:

$$T(t) = T_S \, e^{-t/(3\tau)} \tag{89}$$

$$\rho(t) = \rho_S \, e^{-t/\tau}, \tag{90}$$

where the shock temperature T_S can be defined as in, e.g., (Nadyozhin & Deputovich 2002; Woosley et al. 2002)

$$T_S = 2.4 \, E_{51}^{1/4} \, R_0^{-3/4} \text{ GK}, \tag{91}$$

with the explosion energy E_{51} in 10^{51} erg, and an initial radius R_0 in 10^8 cm. The shock density is given by the jump condition ($\rho_S = 7\rho_0$). For an initial (preshock) density of $\rho_0 = 10^6$ g cm^{-3}, an initial radius of $R_0 = 2 \times 10^8$, and an explosion energy of 10^{52} erg, we obtain

$$T(t) = 2.4 \, (0.2)^{-3/4} \, e^{-t/(3\tau)} \tag{92}$$

$$\rho(t) = 7 \times 10^6 e^{-t/\tau}. \tag{93}$$

When we further assume an electron fraction of $Y_e = 0.498$ as typical in the Si shell, we obtain final abundances that are located around ^{56}Fe (Figure 14).

5.1.4. νp-process

Neutrinos can be crucial to synthesize proton-rich isotopes. If the neutrino flux is strong enough, this can lead to a νp-process. The conditions for this are, for example, fulfilled in the
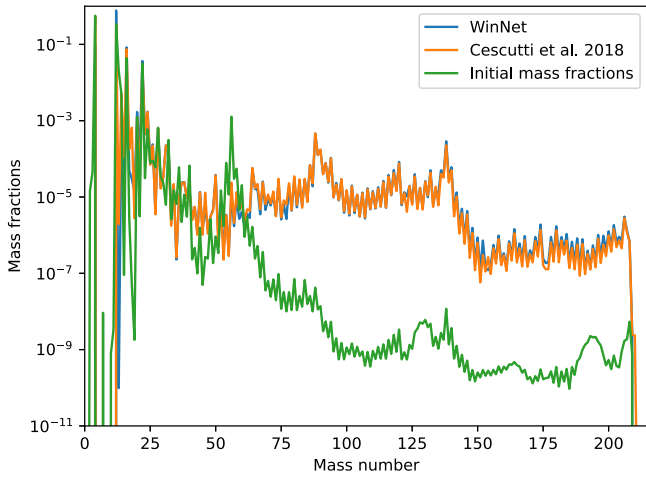
Figure 13. Initial and final mass fractions of a main *s*-process. The trajectory as well as the final mass fractions are taken from Cescutti et al. (2018) accessed via Cescutti (2022).

MRSNe model 35OC-RO of Obergaulinger & Aloy (2017) and Reichert et al. (2021). The nucleosynthetic flow with and without neutrinos is shown in Figure 15.

5.1.5. The Weak r-process

The weak *r*-process, i.e., a synthetization of elements up to the second *r*-process peak ($A \sim 130$) can occur in moderately neutron-enriched environments. These conditions can be found in a variety of astrophysical host scenarios. Here, we show an exemplary trajectory from an MRSNe (Obergaulinger & Aloy 2017; Reichert et al. 2021), the neutrino-driven wind of an NSM (Perego et al. 2014; Martin et al. 2015), and the neutrino-driven wind of a CCSNe (Bliss et al. 2018). The final mass fractions are shown in Figure 16.

5.1.6. Strong r-process

Calculating a full *r*-process is one of the most challenging nuclear reaction network calculations. Here we include ~ 6500 nuclei up to ^{337}Rg. The astrophysical host event of the *r*-process is not fully understood yet. Very promising candidates are NSMs, neutron star–black hole (NSBH) mergers, or MRSNe. For these scenarios, we show the results of individual trajectories in Figure 17. These trajectories come from a variety of (M)HD simulations and were presented in Winteler et al. (2012), Korobkin et al. (2012), Piran et al. (2013), Rosswog (2013), Wu et al. (2016), Bovard et al. (2017), Obergaulinger & Aloy (2017), Reichert et al. (2021), Obergaulinger & Aloy (2021), and Reichert et al. (2023).

5.2. Test Scenarios

We have implemented a series of tests in order to monitor the performance and consistency of WINNET. The tests cover a range of numerical and physical scenarios, which we will present in this section. Many of the tests are designed in a way that an analytic calculation of the result is also possible. Furthermore, we implemented technical test cases such as reading the initial composition, the correct reproduction of the input thermodynamic conditions, and correct implementation of the different reaction rate formats.
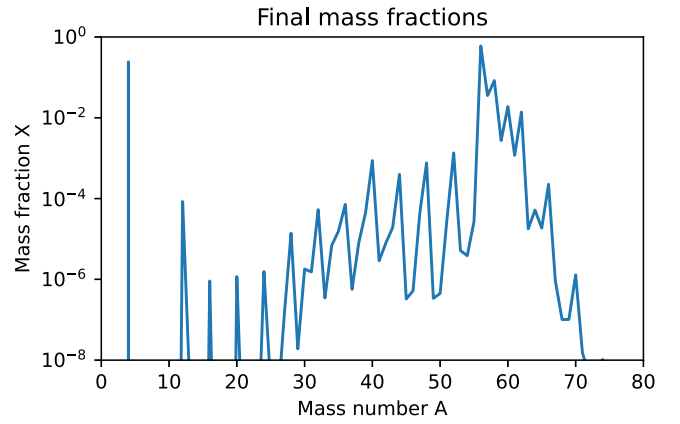
Figure 14. Final mass fractions of complete Si burning obtained with a simple parametric model.
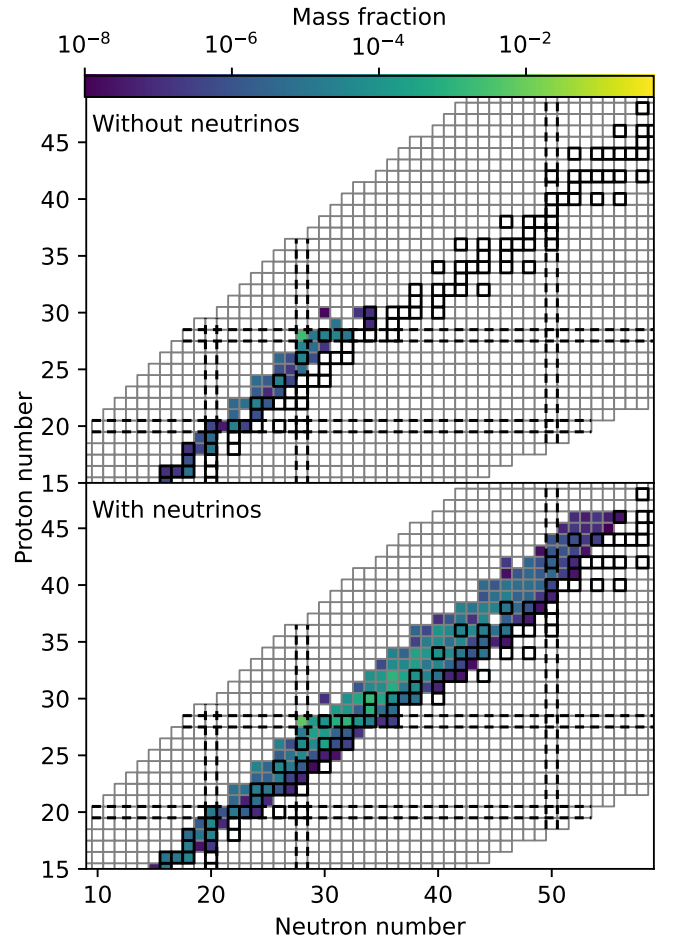
Figure 15. Mass fractions at $t = 1.8 \times 10^3$ s for one trajectory within the MRSNe model 35OC-RO of Obergaulinger & Aloy (2017) and Reichert et al. (2021). Upper panel: calculation without involving neutrino reactions. Lower panel: calculation using neutrino reactions on nucleons as well as on heavier nuclei (Sieverding et al. 2018).

5.2.1. β Decays

A simple nucleosynthesis calculation is given by a β decay. We tested the decay of neutrons to protons, as well as the decay chain of ^{56}Ni. The results give an interesting insight into the accuracy of the integration using an implicit Euler integration scheme. We recall that this scheme does not have any error estimate for the time step and the convergence criterion of the
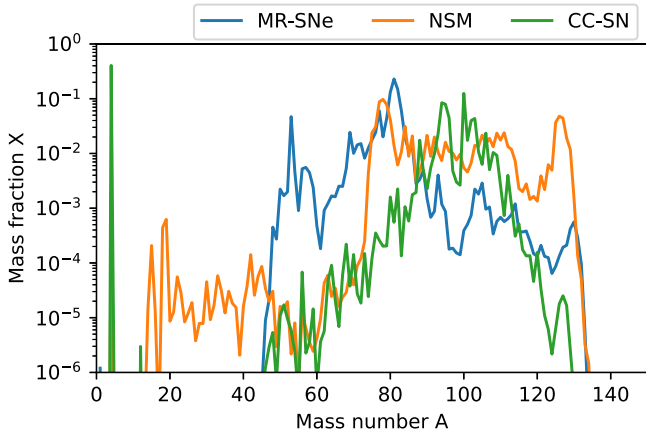
Figure 16. Final mass fractions after 1 Gyr for a trajectory of an MRSNe (Obergaulinger & Aloy 2017, Reichert et al. 2021), of the neutrino-driven wind of an NSM (Perego et al. 2014, Martin et al. 2015), and of the neutrino-driven wind of a CCSNe (Bliss et al. 2018).

mass conservation (i.e., $\sum_i X_i = 1$; Equation (54)). While this is common practice for calculations involving a large amount of nuclei and reactions (e.g., Hix & Thielemann 1999; Lippuner & Roberts 2017), within the tested decays it leads to uncertainties. As an example, we show the time evolution of ^{56}Ni, ^{56}Co, and ^{56}Fe in Figure 18.

The discrepancies between the implicit Euler solution and the analytic solution can be reduced by choosing adapted smaller time steps resulting from smaller ϵ_{Euler} values (in the example, $\epsilon_{\text{Euler}} = 10^{-1}$ was used; see Equation (57)). The example also shows the strength of the adaptive time-step control within the Gear solver, which is able to stay close to the analytic solution.

Another test is based on the β-delayed fission of ^{295}Am. Identical to a normal β decay, we can calculate the decay of this nucleus via

$$Y(t) = Y_0\, e^{-\alpha t}, \tag{94}$$

with the decay constant α. The products of this decay are determined by the fission fragment distribution that can be calculated analytically, as in Kodama & Takahashi (1975) or Panov et al. (2001). Additionally, we include the fission fragment distribution of Mumpower et al. (2020) for β-delayed and neutron-induced fission. This distribution spans a wide range of mass numbers. The different fragments for a simulation time of $t = 10^{-2}$ s are shown in Figure 19.

The calculated abundance pattern deviates less than 1% from the input fission fragment distributions.

5.2.2. Equilibrium Cases

Useful scenarios are cases were an equilibrium value is obtained. An equilibrium situation can be challenging for numerical solvers, as constant abundances appear like a reaction timescale that is approaching infinity (e.g., Hix & Thielemann 1999; Feger 2011; Lippuner & Roberts 2017). In the following, we present the case of an (n, γ)–(γ, n) equilibrium as well as equilibria obtained by electron and positron captures and neutrino absorption.

In the case of an (n, γ)–(γ, n) equilibrium between ^{64}Ni and ^{65}Ni, the analytic solution of the equilibrium composition can
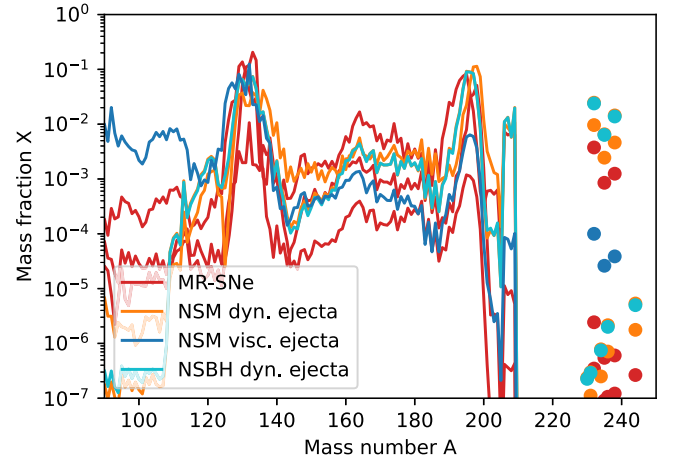
Figure 17. Final mass fractions of various example trajectories. Within MRSNe, the models used in Winteler et al. (2012), Obergaulinger & Aloy (2017), Reichert et al. (2021), Obergaulinger & Aloy (2021), and Reichert et al. (2023) are shown (red lines). For the dynamic ejecta of an NSM (orange lines), we show the simulations of Korobkin et al. (2012), Piran et al. (2013), Rosswog (2013), model ns10ns10, and Bovard et al. (2017). Furthermore, we illustrate the viscous ejecta of an NSM from the calculation of Wu et al. (2016). The dynamic ejecta of an NSBH merger from Korobkin et al. (2012), Piran et al. (2013), Rosswog (2013), and model BH10 is shown as the cyan line.
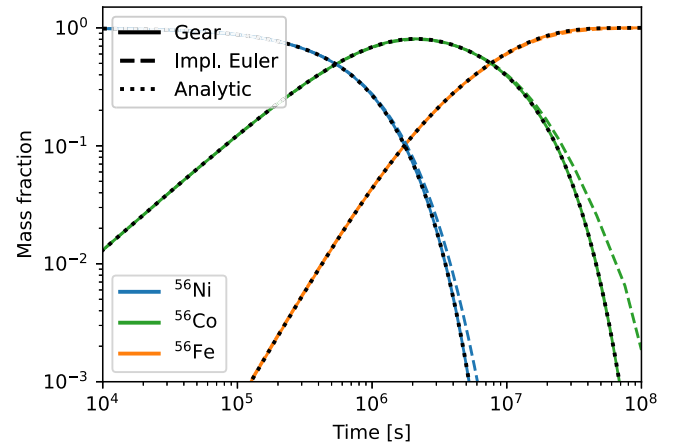
Figure 18. Decay of ^{56}Ni calculated with the Gear (solid line) and implicit Euler solver (dashed line). The analytic solution is shown with the dotted lines.

be derived as

$$Y(n) = \frac{\lambda_{\gamma,n} - \sqrt{\lambda_{\gamma,n}^2 + 4\rho\, N_A\, \langle\sigma\nu\rangle_{n,\gamma}\, \lambda_{\gamma,n}/65}}{-2\rho\, N_A\, \langle\sigma\nu\rangle_{n,\gamma}} \tag{95}$$

$$Y(^{64}\text{Ni}) = Y(n) \tag{96}$$

$$Y(^{65}\text{Ni}) = 1/65 - Y(n). \tag{97}$$

For $T = 8$ GK and $\rho = 10^9$ g cm^{-3} and matter initially consisting out of pure $Y(^{65}\text{Ni})$ (which introduced the factor 1/65), we obtain $Y(n) = Y(^{64}\text{Ni}) = 7.35175 \times 10^{-3}$ and $Y(^{65}\text{Ni}) = 8.03286 \times 10^{-3}$. While the integration with the Gear scheme results in an excellent agreement within 0.0015 %, the time step within the implicit Euler becomes very small. This leads to numerical instabilities and a large deviation from the analytic solution after 10^3 s (see Figure 20). This instability is unlikely to be resolved by more restrictive time steps in the implicit Euler scheme as the time step is based on changes in the thermodynamic conditions or abundances. Since both are
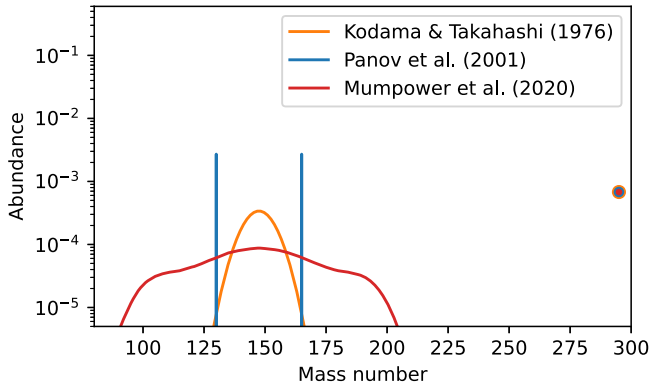
Figure 19. The β-delayed fission of ^{295}Am. Shown are the abundances after 10^{-2} s for three different fission fragment distributions.
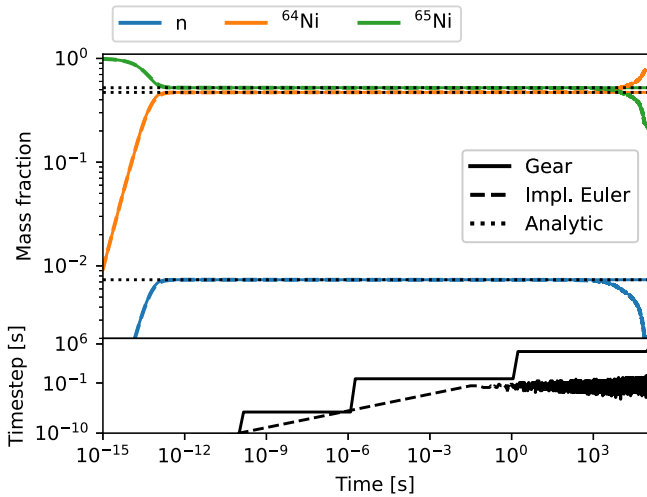
Figure 20. Upper panel: mass fractions of neutrons (blue), ^{64}Ni (orange), and ^{65}Ni (green) for the implicit Euler (dashed line) and Gear integration scheme (solid line). The analytic equilibrium solution is shown with the black dotted lines. Lower panel: the time step of the implicit Euler and Gear integration schemes.
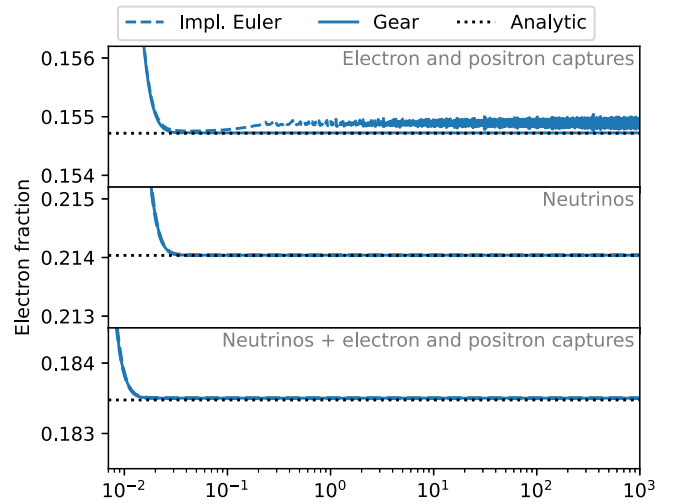

Figure 21. Electron fraction under hydrostatic conditions with $T = 30$ GK and $\rho = 10^{10}$ g cm^{-3}. Upper panel: equilibrium case when involving only electron and positron captures. Middle panel: equilibrium case when involving only neutrinos with luminosities of $L_\nu = 10^{52}$ erg s^{-1}, $L_{\bar\nu} = 5 \times 10^{52}$ erg s^{-1}, and neutrino energies of $E_\nu = 25.2$ MeV as well as $E_{\bar\nu} = 31.5$ MeV.

static, the scheme will always attempt very large (possibly too large) time steps. This continues until large errors have been accumulated and the solution diverges. On the other hand, the Gear solver estimates an integration error, independent of changes in conditions or abundances. As a consequence, the solution is more stable.

Another equilibrium test scenario is given by the equilibrium of electron, positron, and neutrino captures. These equilibria are important to understand the initial electron fraction in r-process calculations. In the following, we investigate the situation of the equilibrium electron fraction when only considering electron/positron captures on nucleons, neutrino absorption on nucleons, and a combination of both.

Similar to Just et al. (2022b), we can calculate the equilibrium electron fractions for all three scenarios. Assuming only electron and positron captures, the equilibrium electron fraction for hydrostatic conditions can be obtained by solving

$$\lambda_{e^+} Y(n) - \lambda_{e^-} Y(p) = 0, \tag{98}$$

with the positron- and electron-capture rate λ_{e^+} and λ_{e^-}, respectively. For a constant temperature of 30 GK and density of 10^{10} g cm^{-3}, we obtain $Y_{e,\,em} = 0.155$. Both integration

schemes obtain great precision, with the Gear solver agreeing within 0.004%, and the implicit Euler agreeing within 0.076%. The implicit Euler integration scheme shows again some numerical noise (upper panel in Figure 21), and the result is therefore slightly worse compared to the Gear integration scheme. For the scenario with only neutrinos irradiating the matter, we can similarly calculate the equilibrium electron fraction

$$\lambda_{\nu_e} Y(n) - \lambda_{\bar\nu_e} Y(p) = 0, \tag{99}$$

with the neutrino and antineutrino cross sections λ_{ν_e} and $\lambda_{\bar\nu_e}$, respectively. Assuming matter located at a radius of 50 km, irradiated by neutrino luminosities of $L_\nu = 10^{52}$ erg s^{-1}, $L_{\bar\nu} = 5 \times 10^{52}$ erg s^{-1}, and neutrino energies of $E_\nu = 25.2$ MeV as well as $E_{\bar\nu} = 31.5$ MeV, we obtain $Y_{e,abs} = 0.214$. The final values of both integration schemes agree within 5×10^{-8} % (middle panel of Figure 21). Combining electron, positron, and neutrino captures, the equilibrium electron fraction can be obtained by solving

$$(\lambda_{\nu_e} + \lambda_{e^+}) Y(n) - (\lambda_{\bar\nu_e} + \lambda_{e^-}) Y(p) = 0. \tag{100}$$

For the conditions assumed here, we obtain $Y_{e,\beta} = 0.1835$, which only deviates by 0.014% from the equilibrium value (lower panel of Figure 21).

Another equilibrium case is given by NSE (Section 2.3). We tested that the transition from the NSE region to the network region is consistent. Therefore, we calculated the NSE composition for $T = 7$ GK, $\rho = 10^7$ g cm^{-3}, and $Y_e = 0.5$ with and without screening. In addition, we calculated the mass fractions after 10^2 s when starting with neutrons and protons only, using the same hydrostatic conditions and strong reactions only. This system should also approach NSE. Again, we calculate the abundances with and without electron screening corrections (see Figure 1). As a consequence of the previous outlined tests, we only calculated the test with the Gear integration method.

Table 3
Final Abundances for Hydrostatic Carbon–Oxygen Test Case

A	Z	Y_{WinNet}	Δ_{SkyNet} $[10^{-2}\%]$	Δ_{ReNet} $[10^{-3}\%]$	Δ_{XNet} $[10^{-1}\%]$
4	2	4.01×10^{-09}	0.82	0.13	0.25
12	6	4.04×10^{-18}	0.53	0.08	0.16
16	8	1.55×10^{-16}	8.06	1.27	2.44
20	10	1.89×10^{-19}	7.23	1.14	2.19
24	12	1.14×10^{-14}	6.61	1.04	2.00
28	14	8.14×10^{-09}	5.79	0.91	1.75
32	16	4.52×10^{-08}	4.96	0.78	1.50
36	18	7.54×10^{-09}	4.13	0.65	1.25
40	20	5.78×10^{-07}	3.31	0.52	1.00
44	22	2.89×10^{-09}	2.48	0.39	0.75
48	24	3.23×10^{-07}	1.65	0.26	0.50
52	26	7.13×10^{-05}	0.82	0.13	0.25
56	28	1.78×10^{-02}	0.003	0.001	0.001

Note. Columns (4)–(6) show the deviation compared to the results of SKYNET, RENET, and XNET, respectively.

5.2.3. Other Tests

If the nuclear reaction network is sufficiently large, deriving an analytic expression for the solution is often not possible anymore. In these cases, it is beneficial to compare the result with other nuclear reaction networks.

We calculate a case of hydrostatic carbon–oxygen burning with $\rho = 10^9$ g cm^{-3} and a temperature of 3 GK for 10^{12} s. The initial composition consisted of $X(^{12}\mathrm{C}) = X(^{16}\mathrm{O}) = 0.5$. In total we involve 13 nuclei in the calculation. We compare the final abundances of WINNET (using Gears integration method) with the results of the nuclear reaction networks SKYNET (Lippuner & Roberts 2017), RENET (Navó et al. 2023), and XNET (Hix & Thielemann 1999).

The final abundances of WINNET deviate by less than 1% to all other reaction networks (Table 3). The abundant nucleus ^{56}Ni even agrees with a maximum deviation of $10^{-4}\%$ only. We note that we did not tune the specific numerical parameters used in the different codes. More restrictive time steps can therefore lead to an even better agreement. To test the implementation of detailed balance (Section 2.2), we repeated the calculation performed in Lippuner & Roberts (2017) with SKYNET. We calculate the nucleosynthesis of a trajectory of an X-ray burst from Schatz et al. (2001). The result of four calculations is shown in Figure 22. There, we use the Reaclib v2.2 and calculate the nucleosynthesis with WINNET using the reverse rates as given by Reaclib (solid orange line). Moreover, we use SKYNET with reverse rates from Reaclib (solid blue line). Additionally, we calculate the same trajectory, but using reverse rates calculated via detailed balance using the Q-value from the mass excess provided within Reaclib (within the winvn file, dashed lines). Both networks agree very well for both cases. The impact of using detailed balance rates with masses from the winvn in contrast to Reaclib reverse rates seems to be larger in SKYNET especially for the smaller mass numbers $\sim$50. However, for both networks, there is also a distinct feature visible at $A \sim 85$.

6. Summary and Conclusion

We have summarized the fundamentals of nuclear reaction networks. The implementation was demonstrated with the single-zone nuclear reaction network code WINNET.
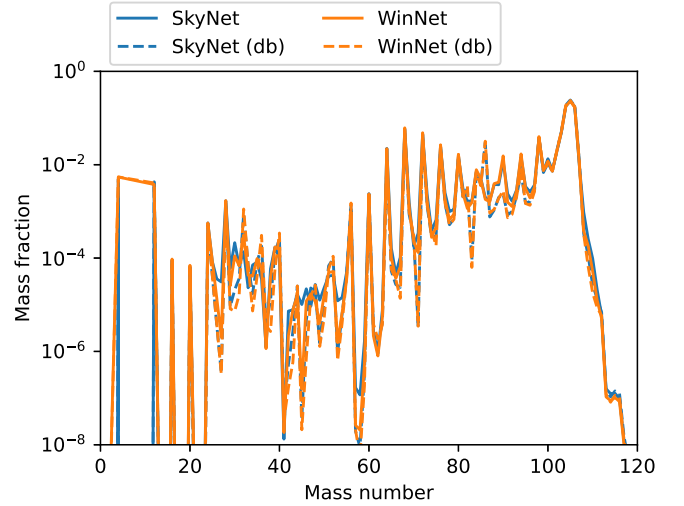
Figure 22. Composition of an X-ray burst (Schatz et al. 2001) after 10^3 s. The result is shown for WINNET (orange lines) and SKYNET (blue lines) with (dashed lines) and without (solid lines) calculating reverse reactions via detailed balance.

We outlined the differential equations that underlie every nuclear reaction network code. Additionally, we presented two implicit numerical techniques to solve these equations, the implicit Euler and Gear's integration scheme.

A mandatory ingredient is also the set of reaction rates. The reaction rates can originate from different databases with varying parameterizations. Hereby, one should ensure that the same underlying nuclear physic inputs such as mass models are used. We described the reaction rate formats that are supported by WINNET, namely the Reaclib reaction rate database, a format for β-delayed neutron emission, tabulated rates, theoretical β^+, β^-, electron-capture and positron-capture rates, neutrino reactions, and fission reactions.

All of these different reaction sources get a different priority assigned, and rates that appear in more than one source are replaced by the rate with the highest priority. This priority is chosen arbitrarily without any estimate of the quality of the rate, and there could be still some action required if a user wants to use specific reaction rates.

WINNET is further able to calculate detailed balance reactions on-the-fly, which can be useful especially for tabulated rates, where a tabulation of the reverse reactions could break the detailed balance principle. If included, the detailed balance reactions will replace all reverse reactions in the other reaction rate sources.

This is also especially useful when implementing new reaction rates for which the reverse rates may not always have been published. As an example, deBoer et al. (2017) published the reaction rate $^{12}\mathrm{C}(\alpha, \gamma)^{16}\mathrm{O}$. While the forward rate can easily be changed as they give Reaclib parameters (Section 4.2.1) and tabulated values (Section 4.2.3), the reverse reaction should also be consistently changed (Section 2.2). Instead of calculating this rate by hand, within WINNET one can enable a parameter to calculate the reverse reaction internally.

All charged particle reaction rates can be further altered by electron screening. This correction is implemented with a multiplicative factor to the reaction rates.

We presented the energy feedback from nuclear reactions onto the temperature, which is implemented in the form of an operator splitting method.

Finally, we introduced simple examples and test cases to demonstrate the reliability of the reaction network code WINNET. Using these test cases, we analyzed the advantages and disadvantages of the different implemented numerical integration methods. We conclude that hydrostatic and equilibrium conditions are often more efficient and precise with the Gear integration method. More complex rapidly varying thermodynamic conditions are more efficient with the implicit Euler integration method.

In addition to the reliability, a large focus during the development of WINNET was the usability. The code provides an easy interface to the user by a simple parameter file. Additionally, comments are written entirely in a doxygen[27] conform format, and the documentation can be accessed along with the code. Due to the modular structure, it is also easy to change the included reactions. Additionally, large effort has been undertaken to supply understandable error messages. To give an example, if an input parameter is misspelled, the error message contains not only that this parameter does not exist, but also points to the most similar existing parameter.

When deciding for or against favoring the usage of WINNET over other publicly available reaction networks, one should keep in mind the advantages and disadvantages for carrying out the desired task. An obvious point to make here is the code language. Users that want to make changes in the code and that are more familiar with C or C++ may feel more comfortable with using NUCNET (Meyer & Adams 2007) or SKYNET (Lippuner & Roberts 2017) rather than the Fortran 90 written codes of TORCH (Paxton et al. 2015), XNET (Hix & Thielemann 1999), or WINNET. For applications that require including the reaction network into a hydrodynamical code, the usage of TORCH or XNET may be favored over WINNET. While it is not impossible to include WINNET into a hydrodynamical code, there is more experience with TORCH or XNET, as both have already been used in hydrodynamical simulations. Furthermore, there has been more effort in parallelizing and optimizing XNET especially when calculating abundances for more than one zone. Since the calculation of the ejecta of astrophysical events often relies on many independent tracer particles, the parallelization of WINNET relies on executing many instances of the reaction network for different tracer particles. No effort has been made in parallelizing the calculation of a single tracer particle, and a single instance of WINNET should always be executed on one CPU only. Similar to XNET and in contrast to SKYNET, WINNET optionally performs an initialization step to bring the included reaction rates into an advantageous shape to minimize the cost of reading them in. Especially when running many tracers, this can reduce the computational cost of the initialization step. In postprocessed applications where neutrinos play a major role, WINNET definitely has advantages, as it is, to our knowledge, the only public code that is able to use publicly available neutrino reactions on heavier nuclei (Section 4.2.4).[28] Furthermore, for conditions that span a large range of temperatures and densities, the scheme to use and replace theoretical electron-capture/positron-capture/β^+/β^- reactions with experimental half-lives contained in the Jina REACLIB database (Section 4.2.5) is an advantage of WINNET. Regarding

calculations of very neutron-rich environments, to our knowledge, TORCH was never run in the context of the r-process. It is possible to include fission reactions and fragment distributions intoXNET (as done in, e.g., Lippuner & Roberts 2017). However, including more complex fragment distributions with hundreds of fission fragments might be challenging and not possible without code changes. To date, also SKYNET includes only a relatively simple fragment distribution with mostly only two fragments plus neutron emission. If one wants to carry out a study with more complex fission fragments, WINNET could be a better choice, as an arbitrary amount of fragments can be included (see Section 4.2.7). Additionally, we included parameterized α decays into WINNET which is an additional, even though possibly small, effort to include into SKYNET or XNET as well. For testing the impact of newly measured reaction rates in different environments, WINNET is also a good choice, since we consider it relatively easy to exchange reaction rates, but also because WINNET already comes with an extensive set of example cases where the impact of certain rates can be directly tested. Also, for storage critical applications, WINNET includes a very flexible way of turning output on and off. This is not easily possible within SKYNET or TORCH without touching the code itself. For example, if one wants to know only the abundances after 1 day, it is possible within WINNET to exclusively output the abundances at this time. Furthermore, WINNET is able to output either ascii, hdf5, or both files, and we therefore consider the code specifically user and beginner friendly. In contrast, SKYNET necessarily needs to have hdf5 packages installed. Ultimately, for numerical studies where the availability of different numerical solvers is desirable, WINNET or XNET are favored over SKYNET, which only includes a backward Euler integration. On the other hand, XNET and SKYNET include more possibilities for the exploration of matrix inversion packages, as WINNET includes only the sparse PARDISO solver. We also briefly tested the performance of WINNET in comparison to SKYNET for an r-process example. In this test, both codes were similarly fast, with WINNET being slightly faster. However, to get a firmer and more quantitative comparison of the performance, a more detailed investigation that covers additional numerical parameters and astrophysical conditions would be necessary.

With this work, WINNET will be fully public and available for download at GitHub[29] and Zenodo (Reichert et al. 2023). This includes not only the code, but also all example and test cases. If you use them, please cite the according publications that can be found in the documentation.

With future works, we plan to extend WINNET by adding more features. As an example, a sensitivity study that uses WINNET may extend it by the scripts and code extensions to perform this task. To give the individual authors of these parts credit, the corresponding work should be cited when someone makes use of a later added feature.

---

[27] https://www.doxygen.nl/index.html

[28] We note that XNET can also contain neutrino reactions on heavier nuclei; the default rate tables are however not publicly available, and one would have to convert the format of the public rate tables.

[29] https://github.com/nuc-astro/WinNet

(ChETEC) and the "International Research Network for Nuclear Astrophysics" (IReNA).

Appendix
Code Convergence

The accuracy of the nucleosynthesis results not only depends on the nuclear input, but also on numerical parameters. In the following, we investigate in more detail the latter error. For this we use a neutron-rich trajectory from an MRSNe of the simulations of Winteler et al. (2012). We use reactions from the Jina Reaclib (Cyburt et al. 2010) with additional α decays from the Viola-Seaborg formula, theoretical weak rates from Langanke & Martínez-Pinedo (2001) that we exchange with experimental reaction rates at 10^{-1} GK. Fission rates have been used as described in Section 4.2.7 with the fragment distribution of Panov et al. (2001).

First we will investigate different values of ϵ_{NR} for the convergence criterion of the root-finding algorithm within the implicit Euler method (Equation (54)). As default in WINNET, we perform at least two root-finding iterations. To avoid a readjustment to smaller and smaller time steps due to a not converged root finding (see Figure 3), we set the maximum amount of allowed root-finding iterations to a large value of 1000.

The final mass fractions of all runs are shown in the upper-left panel of Figure 23, the difference is defined by $\Delta = 1 - \frac{X_1}{X_2}$, where we took X_1 as mass fractions from the run with $\epsilon_{NR} = 10^{-8}$. This is shown in the lower-left panel of Figure 23. The maximum deviation is of the order of $\sim 0.1\%$. Interestingly, it is the iron region that is prone to errors. This part of enhanced errors vanishes completely when not using theoretical weak rates. These rates depend on temperatures as well as densities and can therefore be more challenging to integrate. For values $\epsilon_{NR} > 10^{-7}$, there is no difference visible. This is due to the fact that the mass for these precisions is
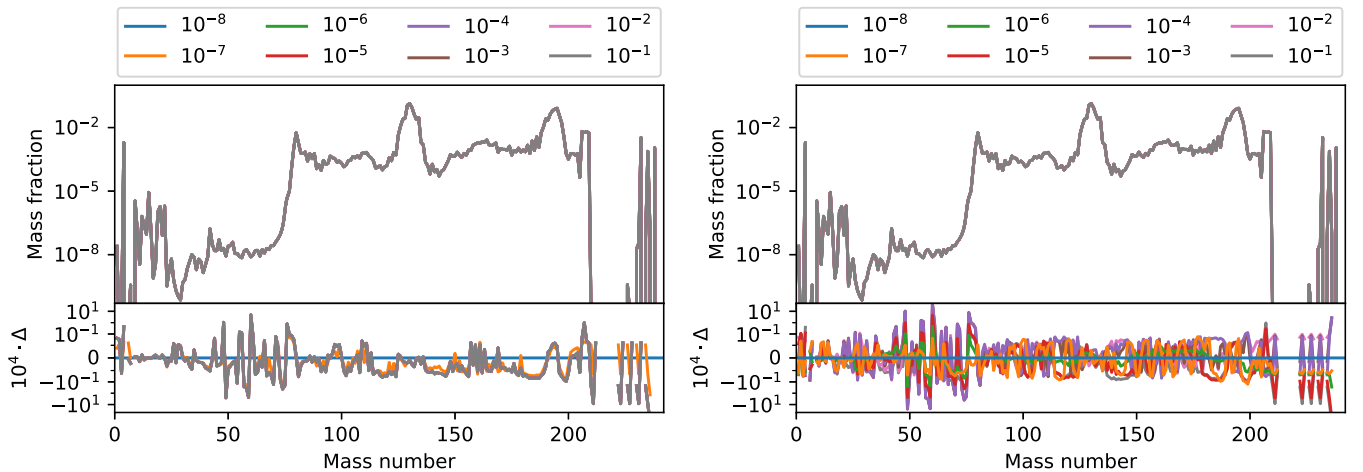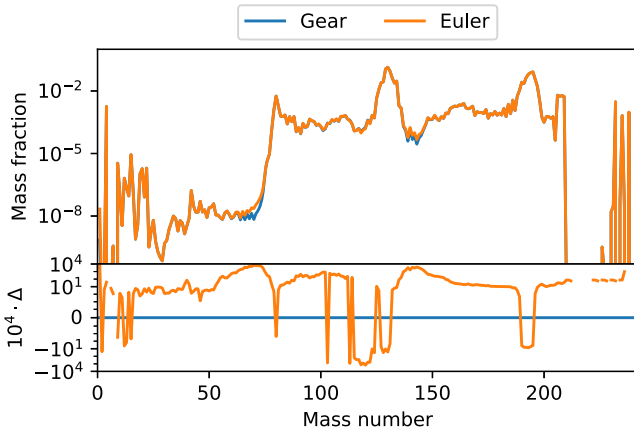

Figure 23. Left plot: calculation using the implicit Euler integration scheme using the Newton–Raphson convergence criteria that is based on baryon conservation (Equation (54)) and different values of ϵ_{NR}. Right plot: the same, but using an alternative convergence criteria of the Newton–Raphson $|\max(\boldsymbol{x}^{k+1}, \boldsymbol{x}^k)/\min(\boldsymbol{x}^{k+1}, \boldsymbol{x}^{k+1}) - 1| < \epsilon_{NR}$. The lower panels show the deviation defined as $\Delta = 1 - \frac{X_1}{X_2}$, using the most restrictive parameters as reference (X_1).
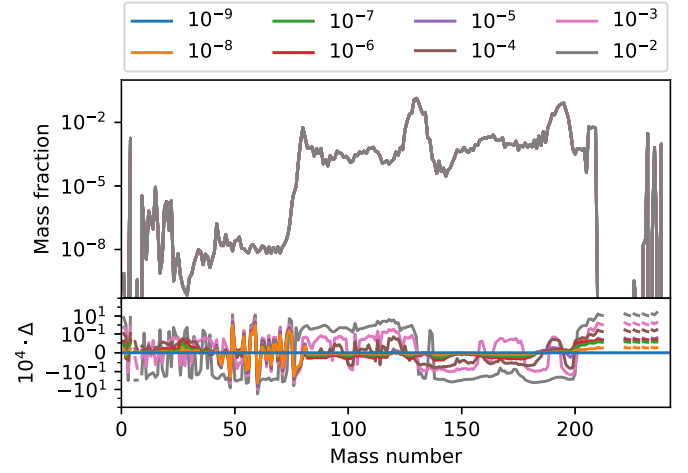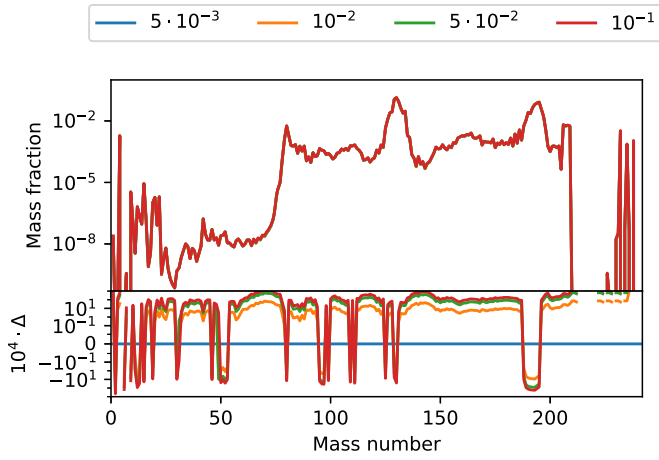
Figure 24. Left plot: calculation using the implicit Euler integration scheme using different time steps by varying ϵ_{Euler} (Equation (57)). Right plot: the same, but using the Gear solver with different time steps by varying ϵ_{Gear}. The lower panels show the deviation defined as $\Delta = 1 - \frac{X_1}{X_2}$, using the most restrictive parameters as reference (X_1).

Figure 25. Comparison of a calculation using the implicit Euler method with $\epsilon_{\text{Euler}} = 5 \times 10^{-3}$ and a calculation using Gear's method with $\epsilon_{\text{Gear}} = 10^{-9}$. We note that the Gear solver in the lower panel is a horizontal line by definition.

already conserved within the minimum of two Newton–Raphson iterations.

An alternative convergence criteria of the Newton–Raphson that is not based on baryon conservation is $|\max(x^{k+1}, x^k)/\min(x^{k+1}, x^{k+1}) - 1| < \epsilon_{\text{NR}}$ for $x^{k+1} > 10^{-10}$. In other words, every abundance should be converged within a given percentage. The result for this convergence criteria is shown in the right panels of Figure 23. Again, the difference between the most restrictive case and the least restrictive one is of the order of ∼0.1%, but the parameter has a much more direct impact on the accuracy. The most restrictive scenarios of both convergence criteria agree even within ∼0.01%, which demonstrates that both criteria can be used interchangeably, and we therefore only include the criterion that is based on baryon conservation, as it has a better performance.

All previous calculations were done with the same time step factor of $\epsilon_{\text{Euler}} = 0.1$ (Equation (57)). We reduced this factor and tested values of 5×10^{-2}, 1×10^{-2}, and 5×10^{-3}. As shown in the left panels of Figure 24, the abundances are converged within ∼10%. In practice, it is not feasible to use a factor of $\epsilon_{\text{Euler}} = 5 \times 10^{-3}$ when calculating many trajectories

(see ∼3000 versus ∼60,000 time steps for $\epsilon_{\text{Euler}} = 10^{-1}$ and $\epsilon_{\text{Euler}} = 5 \times 10^{-3}$, respectively).

The Gear integration method, on the other hand, estimates the time step in a more sophisticated way, based on integration errors. This error is controlled by ϵ_{Gear} (Equation (70)). When reducing ϵ_{Gear}, one directly controls the numerical error (right panels of Figure 24). The error can be reduced to an almost arbitrary precision, and for all calculated runs it lies within an astonishing precision of ∼0.1%.

Finally, it is interesting to compare the most precise calculation using the Gear solver ($\epsilon_{\text{Gear}} = 10^{-9}$) with the most precise calculation using the implicit Euler method ($\epsilon_{\text{Euler}} = 5 \times 10^{-3}$). This comparison is shown in Figure 25. The difference between the calculation using the Gear solver and the implicit Euler is for most parts within 10%; however, some regions, i.e., around $A \sim 70$ and $A \sim 140$, are differing by a factor of ∼2. However, the largest deviation is visible in the abundance of protons with a factor of 30 showing that the numerical method can also have a strong impact especially on light nuclei such as neutrons, protons, and alphas.

ORCID iDs

M. Reichert https://orcid.org/0000-0001-6653-7538
O. Korobkin https://orcid.org/0000-0003-4156-5342
A. Arcones https://orcid.org/0000-0002-6995-3032
M. Eichler https://orcid.org/0000-0002-4445-8908
C. Fröhlich https://orcid.org/0000-0003-0191-2477
R. Hirschi https://orcid.org/0000-0001-8764-6522
M. Jacobi https://orcid.org/0000-0001-8168-4579
J. Kuske https://orcid.org/0009-0005-5121-7343
G. Martínez-Pinedo https://orcid.org/0000-0002-3825-0131
D. Martin https://orcid.org/0000-0002-1988-9706
T. Rauscher https://orcid.org/0000-0002-1266-0642
F.-K. Thielemann https://orcid.org/0000-0002-7256-9330

References

Aikawa, M., Arnould, M., Goriely, S., Jorissen, A., & Takahashi, K. 2005, A&A, 441, 1195
Aloy, M. Á., & Obergaulinger, M. 2021, MNRAS, 500, 4365
Alpher, R. A., Bethe, H., & Gamow, G. 1948, PhRv, 73, 803
Arcones, A., Martínez-Pinedo, G., Roberts, L. F., & Woosley, S. E. 2010, A&A, 522, A25

Arnett, D. 1996, Supernovae and Nucleosynthesis: An Investigation of the History of Matter from the Big Bang to the Present (Princeton, NJ: Princeton University Press)
Arnett, W. D. 1969, Ap&SS, 5, 180
Arnett, W. D. 1977, ApJS, 35, 145
Arnett, W. D., Meakin, C., Hirschi, R., et al. 2019, ApJ, 882, 18
Arnett, W. D., & Truran, J. W. 1969, ApJ, 157, 339
Arnett, W. D., Truran, J. W., & Woosley, S. E. 1971, ApJ, 165, 87
Arnould, M. 1976, A&A, 46, 117
Arnould, M., Norgaard, H., Thielemann, F. K., & Hillebrandt, W. 1980, ApJ, 237, 931
Aver, E., Olive, K. A., & Skillman, E. D. 2010, JCAP, 2010, 003
Bania, T. M., Rood, R. T., & Balser, D. S. 2002, Natur, 415, 54
Barnes, J., & Metzger, B. D. 2022, ApJL, 939, L29
Basu, D. N., Chowdhury, P. R., & Samanta, C. 2005, PhRvC, 72, 051601
Benz, W., Hills, J. G., & Thielemann, F. K. 1989, ApJ, 342, 986
Bhattacharya, M., & Gangopadhyay, G. 2007, PhLB, 651, 263
Bisterzo, S., Travaglio, C., Wiescher, M., Käppeler, F., & Gallino, R. 2017, ApJ, 835, 97
Bliss, J., Arcones, A., Montes, F., & Pereira, J. 2020, PhRvC, 101, 055807
Bliss, J., Arcones, A., & Qian, Y.-Z. 2018, ApJ, 866, 105
Boesgaard, A. M., & Steigman, G. 1985, ARA&A, 23, 319
Bollig, R., Janka, H. T., Lohs, A., et al. 2017, PhRvL, 119, 242702
Bovard, L., Martin, D., Guercilena, F., et al. 2017, PhRvD, 96, 124005
Bovard, L., & Rezzolla, L. 2017, CQGra, 34, 215005
Bravo, E. 2020, MNRAS, 494, 3037
Bravo, E., & García-Senz, D. 1999, MNRAS, 307, 984
Brown, B. A. 1992, PhRvC, 46, 811
Brown, D. A., Chadwick, M. B., Capote, R., et al. 2018, NDS, 148, 1
Brown, P. N., Byrne, G. D., & Hindmarsh, A. C. 1989, SIAM J. Sci. Stat. Comput., 10, 1038
Broyden, C. G. 1965, MaCom, 19, 577
Bruenn, S. W. 1986, ApJS, 62, 331
Burrows, A. 2013, RvMP, 85, 245
Burrows, A., Reddy, S., & Thompson, T. A. 2006, NuPhA, 777, 356
Busso, M., Vescovi, D., Palmerini, S., Cristallo, S., & Antonuccio-Delogu, V. 2021, ApJ, 908, 55
Byrne, G., & Hindmarsh, A. 1975, ACM Trans. Math. Softw., 1, 71
Cardall, C. Y., & Fuller, G. M. 1997, ApJL, 486, L111
Cescutti, G. 2022, Main s-process, v1.2.1, Zenodo, doi:10.5281/zenodo.6474686
Cescutti, G., Hirschi, R., Nishimura, N., et al. 2018, MNRAS, 478, 4101
Clayton, D. 1968, Principles of Stellar Evolution and Nucleosynthesis (Chicago, IL: Univ. Chicago Press)
Coc, A., & Vangioni, E. 2017, IJMPE, 26, 1741002
Cooke, R. J., Pettini, M., & Steidel, C. C. 2018, ApJ, 855, 102
Curtis, S., Ebinger, K., Fröhlich, C., et al. 2019, ApJ, 870, 2
Cyburt, R. H., Amthor, A. M., Ferguson, R., et al. 2010, ApJS, 189, 240
Cyburt, R. H., Fields, B. D., Olive, K. A., & Yeh, T.-H. 2016, RvMP, 88, 015004
Dan, M., Guillochon, J., Brüggen, M., Ramirez-Ruiz, E., & Rosswog, S. 2015, MNRAS, 454, 4411
Dardelet, L., Ritter, C., Prado, P., et al. 2015, arXiv:1505.05500
deBoer, R. J., Görres, J., Wiescher, M., et al. 2017, RvMP, 89, 035007
Denissenkov, P. A., Herwig, F., Woodward, P., et al. 2019, MNRAS, 488, 4258
Descouvemont, P., Adahchour, A., Angulo, C., Coc, A., & Vangioni-Flam, E. 2004, ADNDT, 88, 203
Dewitt, H. E., Graboske, H. C., & Cooper, M. S. 1973, ApJ, 181, 439
Dillmann, I., Heil, M., Käppeler, F., et al. 2006, in AIP Conf. Proc. 819, Capture Gamma-Ray Spectroscopy and Related Topics, ed. A. Topics & A. Aprahamian (Melville, NY: AIP), 123
Doherty, C. L., Gil-Pons, P., Siess, L., & Lattanzio, J. C. 2017, PASA, 34, e056
Dong, J. M., Zhang, H. F., & Royer, G. 2009, PhRvC, 79, 054330
Dong, T., & Ren, Z. 2005, EPJA, 26, 69
Eggenberger, P., Ekström, S., Georgy, C., et al. 2021, A&A, 652, A137
Eichler, M., Arcones, A., Kelic, A., et al. 2015, ApJ, 808, 30
Erler, J., Langanke, K., Loens, H., Martinez-Pinedo, G., & Reinhard, P.-G. 2012, PhRvC, 85, 025802
Feger, E. D. 2011, PhD thesis, Univ. of Tennessee, https://trace.tennessee.edu/utk_graddiss/1048
Fields, B. D. 2011, ARNPS, 61, 47
Fields, B. D., & Olive, K. A. 2022, JCAP, 2022, 078
Fowler, W. A. 1974, QJRAS, 15, 82
Fowler, W. A., Caughlan, G. R., & Zimmerman, B. A. 1967, ARA&A, 5, 525

Freiburghaus, C., Rosswog, S., & Thielemann, F.-K. 1999, ApJL, 525, L121
Frischknecht, U., Hirschi, R., Pignatari, M., et al. 2016, MNRAS, 456, 1803
Fröhlich, C., Hauser, P., Liebendörfer, M., et al. 2006a, ApJ, 637, 415
Fröhlich, C., Martínez-Pinedo, G., Liebendörfer, M., et al. 2006b, PhRvL, 96, 142502
Fryxell, B., Mueller, E., & Arnett, D. 1991, ApJ, 367, 619
Fujimoto, S.-I., Nishimura, N., & Hashimoto, M.-a 2008, ApJ, 680, 1350
Fuller, G. M., Fowler, W. A., & Newman, M. J. 1982, ApJS, 48, 279
Fuller, G. M., Fowler, W. A., & Newman, M. J. 1985, ApJ, 293, 1
Garcia-Senz, D., Cabezon, R. M., Arcones, A., Relano, A., & Thielemann, F. K. 2013, MNRAS, 436, 3413
García-Senz, D., Cabezón, R. M., Domínguez, I., & Thielemann, F. K. 2016, ApJ, 819, 132
Gear, C. W. 1971, Commun. ACM, 14, 176
Ghosh, S., Wolfe, N., & Fröhlich, C. 2022, ApJ, 929, 43
Gil-Pons, P., Doherty, C. L., Gutiérrez, J. L., et al. 2018, PASA, 35, e038
Giuliani, S. A., Martínez-Pinedo, G., & Robledo, L. M. 2018a, PhRvC, 97, 034323
Giuliani, S. A., Martínez-Pinedo, G., & Robledo, L. M. 2018b, JPhCS, 940, 012013
Giuliani, S. A., Martínez-Pinedo, G., Wu, M.-R., & Robledo, L. M. 2020, PhRvC, 102, 045804
Goriely, S., Bauswein, A., & Janka, H.-T. 2011, ApJL, 738, L32
Goriely, S., Hilaire, S., Koning, A. J., Sin, M., & Capote, R. 2009, PhRvC, 79, 024612
Görres, J., Wiescher, M., & Thielemann, F.-K. 1995, PhRvC, 51, 392
Gronow, S., Côté, B., Lach, F., et al. 2021, A&A, 656, A94
Halevi, G., & Mösta, P. 2018, MNRAS, 477, 2366
Harris, C. R., Millman, K. J., van der Walt, S. J., et al. 2020, Natur, 585, 357
Harris, J. A., Hix, W. R., Chertkow, M. A., et al. 2017, ApJ, 843, 2
Heger, A., Fryer, C. L., Woosley, S. E., Langer, N., & Hartmann, D. H. 2003, ApJ, 591, 288
Heger, A., & Woosley, S. E. 2010, ApJ, 724, 341
Hillebrandt, W., Kromer, M., Röpke, F. K., & Ruiter, A. J. 2013, FrPhy, 8, 116
Hirschi, R., Meynet, G., & Maeder, A. 2004, A&A, 425, 649
Hix, W. R., Khokhlov, A. M., Wheeler, J. C., & Thielemann, F.-K. 1998, ApJ, 503, 332
Hix, W. R., & Meyer, B. S. 2006, NuPhA, 777, 188
Hix, W. R., Parete-Koon, S. T., Freiburghaus, C., & Thielemann, F.-K. 2007, ApJ, 667, 476
Hix, W. R., & Thielemann, F.-K. 1999, JCoAM, 109, 321
Hoffman, R. D., Woosley, S. E., & Qian, Y.-Z. 1997, ApJ, 482, 951
Hoffman, R. D., Woosley, S. E., Weaver, T. A., Rauscher, T., & Thielemann, F. K. 1999, ApJ, 521, 735
Höflich, P., Wheeler, J. C., & Thielemann, F. K. 1998, ApJ, 495, 617
Holmbeck, E. M., Sprouse, T. M., Mumpower, M. R., et al. 2019, ApJ, 870, 23
Holmes, J. A., Woosley, S. E., Fowler, W. A., & Zimmerman, B. A. 1976, ADNDT, 18, 305
Horowitz, C. J. 2002, PhRvD, 65, 043001
Howard, W. M., & Möller, P. 1980, ADNDT, 25, 219
Hunter, J. D. 2007, CSE, 9, 90
Iben, I. J., & Tutukov, A. V. 1984, ApJS, 54, 335
Ichimaru, S. 1993, RvMP, 65, 255
Iliadis, C. 2015, Nuclear Physics of Stars (New York: Wiley-VCH)
Iliadis, C., Champagne, A., José, J., Starrfield, S., & Tupper, P. 2002, ApJS, 142, 105
Itoh, N., Hayashi, H., Nishikawa, A., & Kohyama, Y. 1996, ApJS, 102, 411
Janka, H.-T., Melson, T., & Summa, A. 2016, ARNPS, 66, 341
Jiang, J.-A., Doi, M., Maeda, K., et al. 2017, Natur, 550, 80
Jose, J. 2016, Stellar Explosions: Hydrodynamics and Nucleosynthesis (Boca Raton, FL: CRC Press)
José, J. 2022, Nova Outburst, v1.1.1, Zenodo, doi:10.5281/zenodo.6474694
José, J., & Hernanz, M. 1998, ApJ, 494, 680
José, J., Hernanz, M., Amari, S., Lodders, K., & Zinner, E. 2004, ApJ, 612, 414
Just, O., Aloy, M. A., Obergaulinger, M., & Nagataki, S. 2022a, ApJL, 934, L30
Just, O., Goriely, S., Janka, H. T., Nagataki, S., & Bauswein, A. 2022b, MNRAS, 509, 1377
Kaiser, E. A., Hirschi, R., Arnett, W. D., et al. 2020, MNRAS, 496, 1967
Karakas, A. I., & Lattanzio, J. C. 2014, PASA, 31, e030
Karakas, A. I., & Lugaro, M. 2016, ApJ, 825, 26
Kawano, L., Schramm, D., & Steigman, G. 1988, ApJ, 327, 750
Kelic, A., Valentina Ricciardi, M., & Schmidt, K.-H. 2009, arXiv:0906.4193
Khokhlov, A., Mueller, E., & Hoeflich, P. 1993, A&A, 270, 223
Khokhlov, A. M. 1991, A&A, 245, 114

Khuyagbaatar, J. 2020, NuPhA, 1002, 121958
Kippenhahn, R., Weigert, A., & Weiss, A. 2013, Stellar Structure and Evolution (2nd ed.; Berlin: Springer)
Kobayashi, C., Karakas, A. I., & Lugaro, M. 2020, ApJ, 900, 179
Kodama, T., & Takahashi, K. 1975, NuPhA, 239, 489
Koike, O., Hashimoto, M.-a., Kuromizu, R., & Fujimoto, S.-i. 2004, ApJ, 603, 242
Koning, A. J., Rochman, D., Sublet, J. C., et al. 2019, NDS, 155, 1
Korobkin, O., Rosswog, S., Arcones, A., & Winteler, C. 2012, MNRAS, 426, 1940
Kostka, M., Koning, N., Shand, Z., Ouyed, R., & Jaikumar, P. 2014, A&A, 568, A97
Kotake, K., Takiwaki, T., Suwa, Y., et al. 2012, AdAst, 2012, 428757
Kratz, K. L., Farouqi, K., Mashonkina, L. I., & Pfeiffer, B. 2008, NewAR, 52, 390
Kravchuk, P. A., & Yakovlev, D. G. 2014, PhRvC, 89, 015802
Kullmann, I., Goriely, S., Just, O., et al. 2022, MNRAS, 510, 2804
Kullmann, I., Goriely, S., Just, O., Bauswein, A., & Janka, H. T. 2023, MNRAS, 523, 2551
Kushnir, D., Waxman, E., & Chugunov, A. I. 2019, MNRAS, 486, 449
Lach, F., Callan, F. P., Bubeck, D., et al. 2022, A&A, 658, A179
Langanke, K., & Kolbe, E. 2002, ADNDT, 82, 191
Langanke, K., & Martínez-Pinedo, G. 2001, ADNDT, 79, 1
Leung, S.-C., & Nomoto, K. 2018, ApJ, 861, 143
Leung, S.-C., Nomoto, K., & Suzuki, T. 2020, ApJ, 889, 34
Limongi, M., & Chieffi, A. 2018, ApJS, 237, 13
Lippuner, J., Fernández, R., Roberts, L. F., et al. 2017, MNRAS, 472, 904
Lippuner, J., & Roberts, L. F. 2017, ApJS, 233, 18
Livne, E., & Arnett, D. 1995, ApJ, 452, 62
Longland, R., Martin, D., & José, J. 2014, A&A, 563, A67
MacFadyen, A. I., & Woosley, S. E. 1999, ApJ, 524, 262
Maeda, K., & Terada, Y. 2016, IJMPD, 25, 1630024
Maeder, A., & Meynet, G. 2012, RvMP, 84, 25
Mamdouh, A., Pearson, J., Rayet, M., & Tondeur, F. 2001, NuPhA, 679, 337
Marketin, T., Huther, L., & Martínez-Pinedo, G. 2016, PhRvC, 93, 025805
Martin, D. 2017, PhD thesis, Technical Univ. of Darmstadt
Martin, D., Perego, A., Arcones, A., et al. 2015, ApJ, 813, 2
Martinez-Pinedo, G., Mocelj, D., Zinner, N., et al. 2007, PrPNP, 59, 199
McLaughlin, G. C., & Surman, R. 2005, NuPhA, 758, 189
Meakin, C. A., Seitenzahl, I., Townsley, D., et al. 2009, ApJ, 693, 1188
Meisel, Z., George, S., Ahn, S., et al. 2020, PhRvC, 101, 052801
Mendoza-Temis, J. d. J., Wu, M.-R., Langanke, K., et al. 2015, PhRvC, 92, 055805
Meyer, B. S., & Adams, D. C. 2007, M&PSA, 42, 5215
Mihalas, D., & Weibel-Mihalas, B. 1999, Foundations of Radiation Hydrodynamics (Mineola, NY: Dover)
Miller, J. M., Sprouse, T. M., Fryer, C. L., et al. 2020, ApJ, 902, 66
Mirizzi, A., Tamborra, I., Janka, H. T., et al. 2016, NCimR, 39, 1
Möller, P., Mumpower, M. R., Kawano, T., & Myers, W. D. 2019, ADNDT, 125, 1
Möller, P., Sierk, A. J., Ichikawa, T., Iwamoto, A., & Mumpower, M. 2015, PhRvC, 91, 024310
More, J. J., Garbow, B. S., & Hillstrom, K. E. 1980, User Guide for MINPACK-1 [in FORTRAN] ANL-80-74, Argonne National Lab.
Moscoso, J., de Souza, R. S., Coc, A., & Iliadis, C. 2021, ApJ, 923, 49
Mossa, V., Stöckel, K., Cavanna, F., et al. 2020, Natur, 587, 210
Mösta, P., Roberts, L. F., Halevi, G., et al. 2018, ApJ, 864, 171
Mueller, E. 1986, A&A, 162, 103
Mueller, E., & Arnett, W. D. 1986, ApJ, 307, 619
Müller, B. 2016, PASA, 33, e048
Müller, B. 2020, LRCA, 6, 3
Mumpower, M. R., Jaffke, P., Verriere, M., & Randrup, J. 2020, PhRvC, 101, 054607
Mumpower, M. R., Kawano, T., Sprouse, T. M., et al. 2018, ApJ, 869, 14
Myers, W. D., & Świątecki, W. J. 1999, PhRvC, 60, 014606
Nadyozhin, D. K., & Deputovich, A. Y. 2002, A&A, 386, 711
Nagataki, S., Hashimoto, M.-a., Sato, K., & Yamada, S. 1997, ApJ, 486, 1026
Nakamura, K., Takiwaki, T., Kotake, K., & Nishimura, N. 2014, ApJ, 782, 91
Navó, G., Reichert, M., Obergaulinger, M., & Arcones, A. 2023, ApJ, 951, 112
Nishimura, N., Hirschi, R., Rauscher, T., St., Murphy, J., & Cescutti, G. 2017a, MNRAS, 469, 1752
Nishimura, N., Sawai, H., Takiwaki, T., Yamada, S., & Thielemann, F.-K. 2017b, ApJL, 836, L21
Nishimura, N., Takiwaki, T., & Thielemann, F.-K. 2015, ApJ, 810, 109
Nishimura, S., Kotake, K., Hashimoto, M.-A., et al. 2006, ApJ, 642, 410
Nomoto, K., Thielemann, F.-K., & Miyaji, S. 1985, A&A, 149, 239

Nomoto, K., Thielemann, F.-K., & Yokoi, K. 1984, ApJ, 286, 644
Obergaulinger, M., & Aloy, M. Á. 2017, MNRAS, 469, L43
Obergaulinger, M., & Aloy, M. Á. 2021, MNRAS, 503, 4942
Oda, T., Hino, M., Muto, K., Takahara, M., & Sato, K. 1994, ADNDT, 56, 231
Olive, K. A., Schramm, D. N., Steigman, G., & Walker, T. P. 1990, PhLB, 236, 454
Otsuki, K., Mathews, G. J., & Kajino, T. 2003, NewA, 8, 767
Otsuki, K., Tagoshi, H., Kajino, T., & Wanajo, S.-Y. 2000, ApJ, 533, 424
Pakmor, R., Kromer, M., Taubenberger, S., & Springel, V. 2013, ApJL, 770, L8
Panov, I. V., Freiburghaus, C., & Thielemann, F. K. 2001, NuPhA, 688, 587
Panov, I. V., Kolbe, E., Pfeiffer, B., et al. 2005, NuPhA, 747, 633
Panov, I. V., Korneev, I. Y., Rauscher, T., et al. 2010, A&A, 513, A61
Paxton, B., Marchant, P., Schwab, J., et al. 2015, ApJS, 220, 15
Peebles, P. J. E. 1966, ApJ, 146, 542
Perego, A., Hempel, M., Fröhlich, C., et al. 2015, ApJ, 806, 275
Perego, A., Rosswog, S., Cabezón, R. M., et al. 2014, MNRAS, 443, 3134
Petermann, I., Langanke, K., Martínez-Pinedo, G., et al. 2012, EPJA, 48, 122
Piessens, R., de Doncker-Kapenga, E., & Ueberhuber, C. W. 1983, Quadpack. A Subroutine Package for Automatic Integration (Heidelberg: Springer-Verlag)
Pignatari, M., & Hirschi, R. 2022, Weak s-process, v1.1.1, Zenodo, doi:10.5281/zenodo.6474728
Piran, T., Nakar, E., & Rosswog, S. 2013, MNRAS, 430, 2121
Pitrou, C., Coc, A., Uzan, J.-P., & Vangioni, E. 2018, PhR, 754, 1
Pitrou, C., Coc, A., Uzan, J.-P., & Vangioni, E. 2021, MNRAS, 502, 2474
Planck Collaboration, Ade, P. A. R., Aghanim, N., et al. 2016, A&A, 594, A13
Plewa, T., & Müller, E. 1999, A&A, 342, 179
Potekhin, A. Y., & Chabrier, G. 2000, PhRvE, 62, 8554
Powell, J., Mueller, B., Aguilera-Dena, D. R., & Langer, N. 2023, MNRAS, 522, 6070
Pruet, J., & Fuller, G. M. 2003, ApJS, 149, 189
Pruet, J., Woosley, S. E., & Hoffman, R. D. 2003, ApJ, 586, 1254
Psaltis, A., Arcones, A., Montes, F., et al. 2022, ApJ, 935, 27
Qi, C., Delion, D. S., Liotta, R. J., & Wyss, R. 2012, PhRvC, 85, 011303
Qian, Y.-Z., & Woosley, S. E. 1996, ApJ, 471, 331
Radice, D., Abdikamalov, E., Ott, C. D., et al. 2018, JPhG, 45, 053003
Rauscher, T. 2003, ApJS, 147, 403
Rauscher, T. 2020, Essentials of Nucleosynthesis and Theoretical Nuclear Astrophysics (Bristol: IOP Publishing)
Rauscher, T. 2022, EPJA, 58, 214
Rauscher, T., & Thielemann, F.-K. 2000, ADNDT, 75, 1
Reichert, M. 2021, PhD thesis, Technische Universität, Darmstadt, doi:10.12921/tuprints-00014198
Reichert, M., Obergaulinger, M., Aloy, M. Á., et al. 2023, MNRAS, 518, 1557
Reichert, M., Obergaulinger, M., Eichler, M., Aloy, M. Á., & Arcones, A. 2021, MNRAS, 501, 5733
Reichert, M., Winteler, C., Korobkin, O., et al., 2023 nuc-astro/WinNet: v1.0.2, Zenodo, doi:10.5281/zenodo.8220549
Rembges, F., Freiburghaus, C., Rauscher, T., et al. 1997, ApJ, 484, 412
Romano, D., Tosi, M., Matteucci, F., & Chiappini, C. 2003, MNRAS, 346, 295
Röpke, F. K., Kromer, M., Seitenzahl, I. R., et al. 2012, ApJL, 750, L19
Röpke, F. K., & Sim, S. A. 2018, SSRv, 214, 72
Rosswog, S. 2013, RSPTA, 371, 20272
Rosswog, S., & Korobkin, O. 2022, AnP, in press
Rosswog, S., Piran, T., & Nakar, E. 2013, MNRAS, 430, 2585
Ryan, S. G., Beers, T. C., Olive, K. A., Fields, B. D., & Norris, J. E. 2000, ApJL, 530, L57
Sahu, B., & Bhoi, S. 2016, PhRvC, 93, 044301
Sallaska, A. L., Iliadis, C., Champange, A. E., et al. 2013, ApJS, 207, 18
Salpeter, E. E. 1954, AuJPh, 7, 373
Salpeter, E. E., & van Horn, H. M. 1969, ApJ, 155, 183
Sandoval, M. A., Hix, W. R., Messer, O. E. B., Lentz, E. J., & Harris, J. A. 2021, ApJ, 921, 113
Saxena, G., Aggarwal, M., Singh, D., et al. 2023, JPhG, 50, 015102
Schatz, H., Aprahamian, A., Barnard, V., et al. 2001, NuPhA, 688, 150
Schatz, H., Aprahamian, A., Goerres, J., et al. 1998, PhR, 294, 167
Schatz, H., Toenjes, R., Pfeiffer, B., et al. 2002, ApJ, 579, 626
Schenk, O., & Gärtner, K. 2004, Future Gener. Comput. Syst., 20, 475
Seitenzahl, I. R., Röpke, F. K., Fink, M., & Pakmor, R. 2010, MNRAS, 407, 2297
Shen, K. J., Boubert, D., Gänsicke, B. T., et al. 2018, ApJ, 865, 15
Siegel, D. M., Barnes, J., & Metzger, B. D. 2019, Natur, 569, 241
Sieverding, A., Langanke, K., Martínez-Pinedo, G., et al. 2019, ApJ, 876, 151
Sieverding, A., Martínez-Pinedo, G., Huther, L., Langanke, K., & Heger, A. 2018, ApJ, 865, 143

Sieverding, A., Waldrop, P. G., Harris, J. A., et al. 2023, ApJ, 950, 34
Smith, A. I., Johnson, E. T., Chen, Z., et al. 2023, ApJ, 947, 65
Smith, M. S., Kawano, L. H., & Malaney, R. A. 1993, ApJS, 85, 219
Sobiczewski, A., Patyk, Z., & Ćwiok, S. 1989, PhLB, 224, 1
Sprouse, T. M., Mumpower, M. R., & Surman, R. 2021, PhRvC, 104, 015803
Sukhbold, T., Ertl, T., Woosley, S. E., Brown, J. M., & Janka, H.-T. 2016, ApJ, 821, 38
Surman, R., & McLaughlin, G. C. 2004, ApJ, 603, 611
Suzuki, T., Toki, H., & Nomoto, K. 2016, ApJ, 817, 163
Tamborra, I., Müller, B., Hüdepohl, L., Janka, H.-T., & Raffelt, G. 2012, PhRvD, 86, 125031
Thielemann, F.-K. 1980, PhD thesis, Technische Hochschule Darmstadt
Thielemann, F.-K., Arnould, M., & Hillebrandt, W. 1979, A&A, 74, 175
Thielemann, F.-K., Diehl, R., Heger, A., Hirschi, R., & Liebendoerfer, M. 2018a, in Astrophysics with Radioactive Isotopes, ed. R. Diehl, D. H. Hartmann, & N. Prantzos (Cham: Springer), 173
Thielemann, F.-K., Isern, J., Perego, A., & von Ballmoos, P. 2018b, SSRv, 214, 62
Thielemann, F.-K., Nomoto, K., & Hashimoto, M.-A. 1996, ApJ, 460, 408
Thielemann, F.-K., Nomoto, K., & Yokoi, K. 1986, A&A, 158, 17
Thompson, T. A., Burrows, A., & Meyer, B. S. 2001, ApJ, 562, 887
Tiesinga, E., Mohr, P. J., Newell, D. B., & Taylor, B. N. 2021, RvMP, 93, 025010
Timmes, F. X. 1999, ApJS, 124, 241
Timmes, F. X., & Arnett, D. 1999, ApJS, 125, 277
Timmes, F. X., Hoffman, R. D., & Woosley, S. E. 2000, ApJS, 129, 377
Truran, J. W., Arnett, W. D., & Cameron, A. G. W. 1967, CaJPh, 45, 2315
Truran, J. W., Cameron, A. G. W., & Gilbert, A. 1966a, CaJPh, 44, 563
Truran, J. W., Hansen, C. J., Cameron, A. G. W., & Gilbert, A. 1966b, CaJPh, 44, 151
Vartanyan, D., Coleman, M. S. B., & Burrows, A. 2022, MNRAS, 510, 4689
Vasini, A., Matteucci, F., & Spitoni, E. 2022, MNRAS, 517, 4256
Vassh, N., Vogt, R., Surman, R., et al. 2019, JPhG, 46, 065202
Viola, V., & Seaborg, G. 1966, J. Inorg. Nucl. Chem., 28, 741
Virtanen, P., Gommers, R., Oliphant, T. E., et al. 2020, NatMe, 17, 261
Vonlanthen, P., Rauscher, T., Winteler, C., et al. 2009, A&A, 503, 47
Wagoner, R. V., Fowler, W. A., & Hoyle, F. 1967, ApJ, 148, 3
Walker, T. P., Steigman, G., Schramm, D. N., Olive, K. A., & Kang, H.-S. 1991, ApJ, 376, 51
Wanajo, S., Hirai, Y., & Prantzos, N. 2021, MNRAS, 505, 5862
Wanajo, S., Kajino, T., Mathews, G. J., & Otsuki, K. 2001, ApJ, 554, 578
Wanajo, S., Müller, B., Janka, H.-T., & Heger, A. 2018, ApJ, 852, 40
Wiescher, M., Gorres, J., Thielemann, F.-K., & Ritter, H. 1986, A&A, 160, 56
Winteler, C. 2012, PhD thesis, The Univ. of Basel
Winteler, C., Käppeli, R., Perego, A., et al. 2012, ApJL, 750, L22
Witt, M., Psaltis, A., Yasin, H., et al. 2021, ApJ, 921, 19
Woosley, S. E., Arnett, W. D., & Clayton, D. D. 1973, ApJS, 26, 231
Woosley, S. E., & Heger, A. 2006, ApJ, 637, 914
Woosley, S. E., Heger, A., & Weaver, T. A. 2002, RvMP, 74, 1015
Woosley, S. E., Taam, R. E., & Weaver, T. A. 1986, ApJ, 301, 601
Woosley, S. E., & Weaver, T. A. 1995, ApJS, 101, 181
Wu, M.-R., Barnes, J., Martínez-Pinedo, G., & Metzger, B. D. 2019, PhRvL, 122, 062701
Wu, M.-R., Fernández, R., Martínez-Pinedo, G., & Metzger, B. D. 2016, MNRAS, 463, 2323
Xu, Y., Takahashi, K., Goriely, S., et al. 2013, NuPhA, 918, 61
Yakovlev, D. G., Gasques, L. R., Afanasjev, A. V., Beard, M., & Wiescher, M. 2006, PhRvC, 74, 035803
Yakovlev, D. G., & Shalybkov, D. A. 1989, ASPRv, 7, 311
Yang, J., Turner, M. S., Steigman, G., Schramm, D. N., & Olive, K. A. 1984, ApJ, 281, 493
Zenati, Y., Siegel, D. M., Metzger, B. D., & Perets, H. B. 2020, MNRAS, 499, 4097